Geophysical Journal International

Geophys. J. Int. (2022) **230,** 932–956
Advance Access publication 2022 March 22
GJI Geodynamics and Tectonics

https://doi.org/10.1093/gji/ggac102

Fully compressible convection for planetary mantles

Yanick Ricard [1], Thierry Alboussière,[1] Stéphane Labrosse [1], Jezabel Curbelo[2] and Fabien Dubuffet[1]

[1] *Ecole normale supérieure de Lyon, UCBL, CNRS, Laboratoire LGLTPE,* 15 parvis René Descartes, Lyon, *France E-mail*ricard@ens-lyon.fr
[2] *Departament de Matemàtiques, Universitat Politècnica de Catalunya, Avda. Diagonal* 647, 08028 *Barcelona, Spain*

Accepted 2022 March 9. Received 2022 March 5; in original form 2021 October 25

SUMMARY

The numerical simulations of convection inside the mantle of the Earth or of terrestrial planets have been based on approximate equations of fluid dynamics. A common approximation is the neglect of the inertia term which is certainly reasonable as the Reynolds number of silicate mantles, or their inverse Prandtl number, are infinitesimally small. However various other simplifications are made which we discuss in this paper. The crudest approximation that can be done is the Boussinesq approximation (BA) where the various parameters are constant and the variations of density are only included in the buoyancy term and assumed to be proportional to temperature with a constant thermal expansivity. The variations of density with pressure and the related physical consequences (mostly the presence of an adiabatic temperature gradient and of dissipation) are usually accounted for by using an anelastic approximation (AA) initially developed for astrophysical and atmospheric situations. The BA and AA cases provide simplified but self-consistent systems of differential equations. Intermediate approximations are also common in the geophysical literature although they are invariably associated with theoretical inconsistencies (non-conservation of total energy, non-conservation of statistically steady state heat flow with depth, momentum and entropy equations implying inconsistent dissipations). We show that, in the infinite Prandtl number case, solving the fully compressible (FC) equations of convection with a realistic equation of state (EoS) is however not much more difficult or numerically challenging than solving the approximate cases. We compare various statistical properties of the Boussinesq, AA and FC simulations in 2-D simulations. We point to an inconsistency of the AA approximation when the two heat capacities are assumed constant. We suggest that at high Rayleigh number, the profile of dissipation in a convective mantle can be directly related to the surface heat flux. Our results are mostly discussed in the framework of mantle convection but the EoS we used is flexible enough to be applied for convection in icy planets or in the inner core.

Key words: Equations of state; Mantle processes; Numerical modelling; Planetary interiors; Dynamics: convection currents, and mantle plumes; Heat generation and transport.

1 INTRODUCTION

The equations of fluid dynamics that control the fully compressible (FC) convection are also the same equations that control the propagation of sound waves. In most geophysical cases, the huge difference of timescales between convection velocities and sound celerity makes an exact numerical simulation impracticable. Various levels of approximations are therefore usually considered. The earliest, most extreme and well known approximation is the Oberbeck–Boussinesq approximation (BA), where the density of the fluid is uniform except in the buoyancy term (Oberbeck 1879; Boussinesq 1903). Some parameters of the equations are sometimes varied (i.e. the thermal expansivity, the thermal conductivity, the viscosity, etc.) while the density is still assumed uniform in the mass and energy conservation equations. We will call these approximations as quasi-Boussinesq, QB (sometimes called extended Boussinesq, King *et al.* 2010). These approximations, BA or QB, are not thermodynamically consistent as the density cannot be uniform if the buoyancy is non-uniform. Furthermore, the thermodynamic Maxwell relations imply that the effect of thermal expansion causes not only the thermal buoyancy but also the adiabatic compression. In geophysical and astrophysical situations (interiors of stars and planets, oceans and atmospheres), compressibility is an essential ingredient and the variations of density are rather controlled by pressure than by temperature. To avoid the propagation of sound waves in the convective medium, the anelastic approximation (AA) has been introduced. The approximation was initially proposed for situations with large Reynolds

numbers such as the atmosphere (Ogura & Phillips 1962), the liquid core (Braginsky & Roberts 1995) or the stars (Lantz & Fan 1999) and was later applied to low Reynolds number situations. The rich bibliography of numerical studies of convection applied to planetary interiors is based on Boussinesq models (e.g. Blankenbach *et al.* 1989; Busse *et al.* 1994; Bunge *et al.* 1997; Parmentier & Sotin 2000; Choblet *et al.* 2007; Zhong *et al.* 2008) or anelastic models (e.g. Jarvis & McKenzie 1980; Glatzmaier 1988; Bercovici *et al.* 1989, 1992; Tackley 2008; Rolf *et al.* 2012; Kameyama & Yamamoto 2018). A comprehensive presentation of the fluid dynamic equations and their approximations when they are applied to planetary interiors is found in Schubert *et al.* (2001).

The basic assumption of the AA, is that the bulk of the convective fluid is well mixed and in a thermodynamic state close to isentropy. The equations are thus expressed as an expansion of the thermodynamic variables around the isentropic state (usually coined as the 'adiabatic state'). The AA can itself be subdivided into various levels of approximations depending on the terms kept in the expansion (Schubert *et al.* 2001; Anufriev *et al.* 2005). The thermodynamic consistency of these AA equations has been discussed in several papers (e.g. Leng & Zhong 2008; King *et al.* 2010; Trubitsyn & Trubitsyn 2015; Verhoeven *et al.* 2015; Yoshida 2017; Gassmoller *et al.* 2020), and below, we will come back to this point in more details. However, we think that the papers on AA convection applied to the mantle have used assumptions on the equation of state (EoS) or on the thermodynamic parameters that are not entirely appropriate for a terrestrial planet. For example, a well-known ingredient of compressible convection is the presence of an adiabatic temperature gradient; a fluid parcel entrained in a descending flow undergoes a temperature increase during adiabatic compression, and a temperature decrease in upwellings. However the adiabatic gradient is expected to decrease with pressure (hence with depth) for any EoS appropriate for a planetary interior while assumptions on the constancy of some parameters made in the available simulations imply rather an increase of the adiabatic gradient with depth (this is the case for all the simulations of the benchmark paper of King *et al.* 2010). This may become problematic particularly when considering large exoplanets in which the pressure is very large. In addition, it remains very difficult to know exactly what are the aspects of convection that may be missed when the AA equations are used instead of the FC formalism.

In this paper, we consider convection in silicate planetary mantles. However some of our results would also apply in liquid or solid metallic layers (core or inner core) and icy satellites and their possible inner oceans (with the appropriate addition of their specific characteristics such as the presence of Coriolis and magnetic forces). Starting from a realistic EoS for the mantle, which seems to be flexible enough to be applied to metallic or icy layers, we show that solving the equations of FC convection at infinite Prandtl number, is feasible and not much more difficult than solving the approximate equations. Moreover, it allows us to assess the appropriateness of approximate models, to discuss the mechanisms of heat transfer and to suggest a profile of dissipation at high Rayleigh number.

2 MURNAGHAN EOS FOR PLANETARY INTERIORS

2.1 Basic thermodynamics

A very important quantity in the thermodynamics of planetary materials is the Grüneisen parameter

$$\Gamma = \frac{\alpha K_T}{\rho C_V} = \frac{1}{\rho C_V}\left(\frac{\partial P}{\partial T}\right)_V, \tag{1}$$

where P, T, α, K_T, ρ and C_V are the pressure, temperature, thermal expansivity, isothermal incompressibility, density and heat capacity at constant volume. The Grüneisen parameter is dimensionless and can reasonably be considered as independent of the temperature at first order (Anderson 2000). An empirical law (Anderson 1979) relates Γ to density,

$$\Gamma = \Gamma_0 \left(\frac{\rho_0}{\rho}\right)^q, \tag{2}$$

where q is around 1, ρ_0 is a reference density and Γ_0 is the Grüneisen parameter at standard conditions. On average, the Grüneisen parameter is between 1 and 2 in the mantle (e.g. Stacey & Davis 2004) or in the core (Alfe *et al.* 2002). The Grüneisen parameter can also be related to the microscopic vibrational properties of crystals (Stacey 1977). At high temperature, above the Debye temperature, all solids have more or less the same heat capacity at constant volume $C_{Vm} = 3R$ per mole of atoms, independent of the nature of the material (R is the gas constant). This approximated rule was proposed by Petit & Dulong (1819). From the typical mole per unit mass of the mantle, $C_V = 1247$ J K^{-1} kg^{-1} [the $3R$ rule seems also to hold approximately for the liquid core, Gubbins *et al.* (2003)]. The approximate constancy of C_V and the fact that Γ is only a function of ρ allow us to integrate (1) as

$$P = F(\rho) + \alpha_0 K_T^0 (T - T_0)\left(\frac{\rho}{\rho_0}\right)^{1-q}, \tag{3}$$

where α_0 and K_T^0 are the thermal expansivity and incompressibility at standard conditions (that we choose to be $P_0 = 0$ Pa, $T_0 = 273$ K) and where $F(\rho)$ is a density dependent integration constant. A rather simple but acceptable choice for the function $F(\rho)$, is the Murnaghan EoS (Murnaghan 1951) at constant T that allows us to write an EoS for solids of the form

$$P = \frac{K_T^0}{n}\left[\left(\frac{\rho}{\rho_0}\right)^n - 1\right] + \alpha_0 K_T^0 (T - T_0)\left(\frac{\rho}{\rho_0}\right)^{1-q}. \tag{4}$$

The exponent n expresses the variations of K_T with pressure at reference temperature T_0 as $K_T(P, T_0) = K_T^0 + nP$. The value of n (also sometimes referred to as K_0') is ≈3−4 for most mantle materials (Stixrude & Lithgow-Bertelloni 2005). Eq. (4) has been used implicitly in various models of mantle convection (e.g. Glatzmaier 1988; Bercovici *et al.* 1989, 1992; Bunge *et al.* 1997). It can easily be used to derive any thermodynamic property like the thermal expansion coefficient $\alpha(P, T)$ or the incompressibility $K_T(P, T)$.

Mayer's relation between the two heat capacities $C_P - C_V = T(\partial P/\partial T)_V(\partial V/\partial T)_P$ will be useful later. It can be straightforwardly deduced from the definitions of the heat capacities using the chain rule for partial derivatives. Introducing the Grüneisen parameter, this relation writes

$$C_P = C_V(1 + \Gamma\alpha T). \tag{5}$$

Since $\Gamma \approx 1$ and $\alpha T \ll 1$, the two heat capacities are very close together although we will argue that this difference should not be neglected (see also Alboussière & Ricard 2013).

2.2 The adiabatic profiles

When convection is vigorous, the motion of fluid parcels is fast enough so that heat diffusion becomes negligible. In the absence of local sources of entropy (when the presence of radiogenic sources and the viscous dissipation are ignored) the temperature of an ascending or descending parcel is only changed by adiabatic expansion or compression. This hypothetic isentropic state is classically called the hydrostatic adiabatic state. In this situation, the thermodynamic variables denoted with a subscript a are solutions of the following equations:

$$\frac{\mathrm{d}\ln\rho_a}{\mathrm{d}z} + \frac{\alpha_a g}{\Gamma_a C_P^a} = 0, \tag{6a}$$

$$\frac{\mathrm{d}\ln T_a}{\mathrm{d}z} + \frac{\alpha_a g}{C_P^a} = 0, \tag{6b}$$

$$\frac{\mathrm{d}P_a}{\mathrm{d}z} + \rho_a g = 0, \tag{6c}$$

z being the vertical coordinate (directed against gravity $g = -g\mathbf{e}_z$).

Since the Grüneisen parameter (2) is only density-dependent, by combination of (6a) and (6b), one gets

$$T_a = T_a^0 \exp\left\{\frac{\Gamma_0}{q}\left[\left(\frac{\rho_0}{\rho_a^0}\right)^q - \left(\frac{\rho_0}{\rho_a}\right)^q\right]\right\}, \tag{7}$$

(or $T_a = T_a^0(\rho/\rho_a^0)^{\Gamma_0}$ in the specific case $q = 0$) where T_a^0 is the surface adiabatic temperature, also called the foot of the adiabat, and ρ_a^0 the surface adiabatic density (i.e. the density at T_a^0 and zero pressure). As α_a can be obtained from the EoS (4) as a function of T_a and ρ_a, as C_P^a is then given by (5), the three adiabatic profiles, solutions of (6a), (6b) and (6c), can be obtained numerically as soon as a surface adiabatic temperature is chosen.

If we apply eq. (7) to the whole Earth mantle from the surface to the core–mantle boundary (CMB) with, for example $\Gamma_0 = q = 1$, $\rho_0 \approx \rho_a^0 = 3200\ \mathrm{kg\ m^{-3}}$, $\rho_a^{\mathrm{CMB}} = 5500\ \mathrm{kg\ m^{-3}}$ and a surface adiabatic temperature $T_a^0 = 1600$ K, we predict a mantle adiabatic temperature increasing by a factor 1.52 from the surface to the CMB (i.e. $T_a^{CMB} = 2432$ K). Of course the actual CMB temperature is obtained by adding to this adiabatic estimate the non-adiabatic temperature increase through the bottom boundary layer of the mantle, likely ≥1300 K, (see e.g. Boehler 1993), indicating a temperature for the top of the core of about 4000 K.

2.3 Validity of the Murnaghan EoS based on the comparison with seismic observations

The different convecting layers of the Earth, mantle, core or inner core are not strictly adiabatic (see e.g. Bunge *et al.* 2001) but should not be far from it. We can therefore check that the EoS (4) is in agreement with the seismologic profile inside the Earth, in both cases where the temperature follows the adiabatic profile (7) computed with $q = 0$ or with $q = 1$. The fit to the Preliminary Reference Earth Model (PREM) is tested for the lower mantle in Fig. 1 and is very precise. We have assumed an adiabatic temperature on top of the lower mantle of 1970 K (Katsura *et al.* 2010). Note that the same EoS is flexible enough to also give an accurate fit to the pressure–density relations in the fluid core or the inner core (Fig. 2a). The corresponding adiabatic temperatures (Fig. 2b) are also in agreement with what is commonly accepted from mineralogical experiments at 670 km depth (Katsura *et al.* 2010), at the CMB (Boehler 1993) or at the core/inner core phase change (Anzellini *et al.* 2013).

Although the pressure-density of PREM can be obtained with either $q = 0$ or $q = 1$ in (4), the choice of q has a stronger effect on the thermal expansivity (see Fig. 3). However the experimentalists do not provide a very stringent criterion to prefer one of the two values as shown by the various observations reported in Fig. 3 (Anderson *et al.* 1992; Brown & Shankland 1981; Chopelas & Boehler 1992; Duffy & Ahrens 1993; Funamori *et al.* 1996; Wolf *et al.* 2015). In the following, we will therefore use $q = 1$ which is a reasonable assumption that simplifies the equations (although for a modest increase in the algebra complexity, $q \neq 1$ could be considered). The pressure is therefore given by

$$P = \frac{K_T^0}{n}\left[\left(\frac{\rho}{\rho_0}\right)^n - 1\right] + \alpha_0 K_T^0(T - T_0), \tag{8}$$

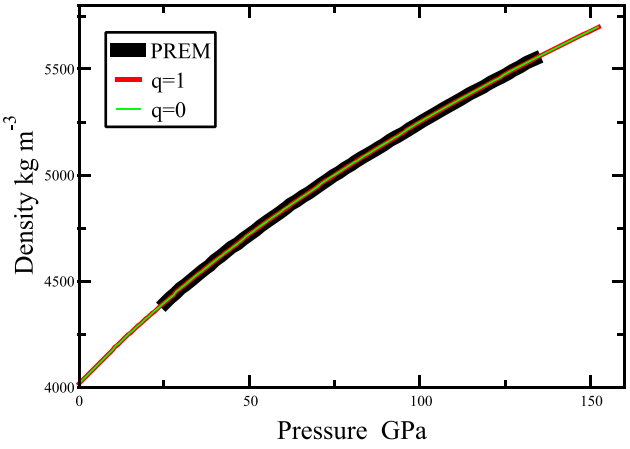

Figure 1. Density as a function of pressure in the lower mantle. The three curves, PREM (thick black) and the predictions using (4) and (7) with $q = 0$ (green) or $q = 1$ (red) are all superimposed. When $q = 1$ we use $\rho_0 = 4180$ kg m^{-3}, $K_0 = 256$ GPa, $n = 3.29$, $T_a^0 = 1849$ K, $\Gamma_0 = 1.22$. When $q = 0$ we use $\rho_0 = 4173$ kg m^{-3}, $K_0 = 244$ GPa, $n = 3.26$, $T_a^0 = 1847$ K, $\Gamma_0 = 1.17$.

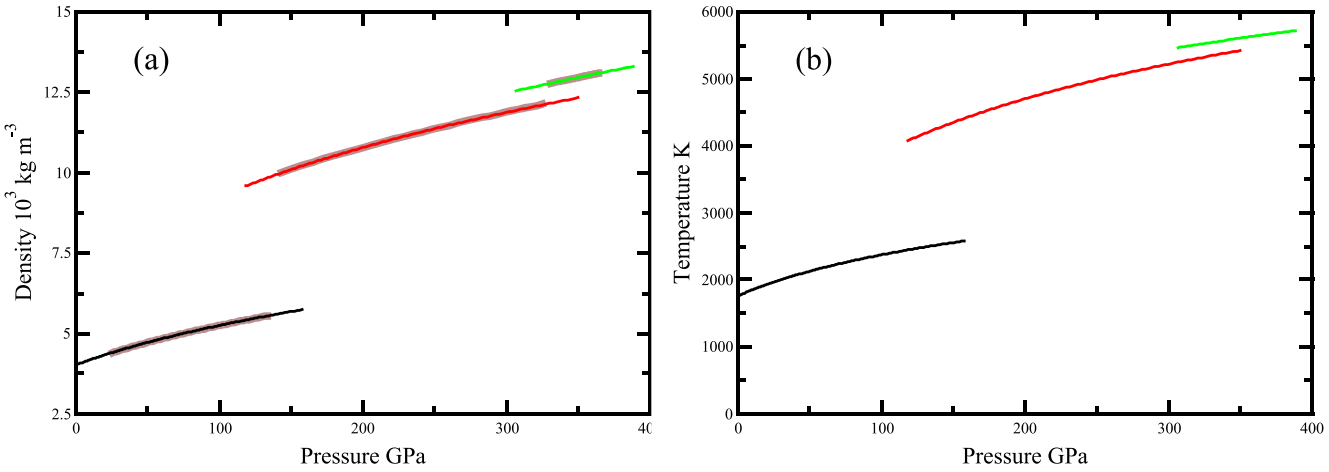

Figure 2. Density as a function of pressure in the Earth according to PREM (thick grey line, panel a). Very accurate adiabatic fits can be obtained using (4) and (11) with $q = 1$. For the lower mantle (thin black) the EoS uses the values of Fig. 1, for the liquid core (red) we use $\rho_0 = 7900$ kg m^{-3}, $K_0 = 210$ GPa, $n = 4.2$, $\Gamma_0 = 1.5$ and for the inner core (green) $\rho_0 = 7913$ kg m^{-3}, $K_0 = 175$ GPa, $n = 4.0$, $\Gamma_0 = 1.25$. The adiabatic temperatures extrapolated at zero pressure are 1970, 3150 and 3450 K, respectively. The corresponding adiabatic temperatures (panel b) correspond to what has been suggested by mineralogical experiments.

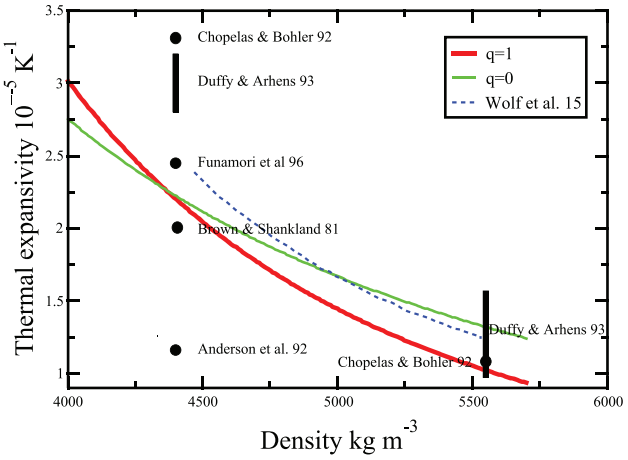

Figure 3. Thermal expansivity α_a as a function of density in the Earth mantle using the parameters of Fig. 1. The predictions are with $q = 1$ (solid red) and $q = 0$ (green). Various experimental observations with conditions appropriate for the top of the lower mantle or for the CMB are indicated by dots or vertical ranges.

which allows us to express the density with the simple equation,

$$\rho = \rho_0 \left[1 + n \left(\frac{P}{K_T^0} - \alpha_0 (T - T_0) \right) \right]^{\frac{1}{n}}. \tag{9}$$

From this EoS, the incompressibility and thermal expansivity coefficients are easily deduced

$$K_T = K_T^0 \left(\frac{\rho}{\rho_0} \right)^n, \tag{10a}$$

$$\alpha = \alpha_0 \left(\frac{\rho_0}{\rho} \right)^n, \tag{10b}$$

and therefore $\alpha K_T = \alpha_0 K_T^0$ is a constant. The adiabatic temperature (7) expressed as a function of density, becomes

$$T_a = T_a^0 \exp \left[\Gamma_0 \left(\frac{\rho_0}{\rho_a^0} - \frac{\rho_0}{\rho_a} \right) \right], \tag{11}$$

where the adiabatic density at the surface ρ_a^0, from (9), is

$$\rho_a^0 = \rho_0 \left(1 - n\alpha_0 (T_a^0 - T_0) \right)^{1/n}. \tag{12}$$

The surface density is of the same order but smaller than ρ_0 as the surface adiabatic temperature is larger than T_0.

The EoS also implies simple expressions for the entropy $\mathcal{S}$ and the enthalpy $\mathcal{H}$, expressions that we will need in discussing the convection equations. Using the differentials $T\mathrm{d}\mathcal{S} = C_V \mathrm{d}T - \alpha K_T T \mathrm{d}\rho/\rho^2$ (see e.g. Ricard 2015) and $\mathrm{d}\mathcal{H} = T\mathrm{d}\mathcal{S} + \mathrm{d}P/\rho$, we obtain

$$\mathcal{S} = A_{\mathcal{S}} + C_V \ln T + \frac{\alpha_0 K_T^0}{\rho}, \tag{13a}$$

$$\mathcal{H} = A_{\mathcal{H}} + \left(C_V + \frac{\alpha_0 K_T^0}{\rho} \right) T + \frac{K_T^0}{(n-1)} \frac{\rho^{n-1}}{\rho_0^n}, \tag{13b}$$

where $A_{\mathcal{S}}$ and $A_{\mathcal{H}}$ are two integration constants that will be discussed later.

2.4 Approximate expressions of the adiabatic profiles

In the simulations (see below), we compute the adiabatic profiles from the exact expressions (6a), (6b) and (6c). However, it is useful to derive approximate forms of these profiles, in particular to discuss implications when considering planets with thicker, hotter or colder mantles than the Earth. As C_P^a and C_V^a only differ by a few per cent [as $(C_P^a - C_V^a)/C_V^a = \Gamma_0 \alpha_0 T_a (\rho_0/\rho_a)^{n+1} \ll 1$, see eq. (5)] adiabatic profiles can be obtained analytically by identifying the two heat capacities and assuming that g is uniform which is roughly the case for the Earth mantle. The approximate solution of eq. (6a) becomes

$$\rho_a = \rho_a^0 \left(1 + \frac{H - z}{h} \right)^{1/(n-1)}, \tag{14}$$

where z is measured from the bottom of the mantle $z = 0$ to the surface $z = H$, and

$$h = \frac{1}{n-1} \frac{K_T^0}{\rho_0 g} \left(\frac{\rho_a^0}{\rho_0} \right)^{n-1}. \tag{15}$$

For the Earth, $h \approx 2500$ km.

The pressure deduced from (6c) is then

$$P_a = \frac{n-1}{n} \rho_a^0 g h \left[\left(\frac{\rho_a}{\rho_a^0} \right)^n - 1 \right], \tag{16}$$

and the temperature remains given by (11) so that both pressure and temperature are direct functions of ρ_a (14).

Assuming that the adiabatic density is given by (14), the ρ_a, P_a and T_a profiles, for a mantle of arbitrary thickness of 3500 km and a uniform gravity comparable to that at Earth's surface, are shown in Fig. 4 using the numerical values of Fig. 1. Although the choice of the EoS parameters is in perfect agreement with the lower mantle of PREM, these depth dependent profiles are not exactly similar to the Earth profiles deduced from seismology (black thick lines of Fig. 4) as the EoS does not account for the upper mantle phase transitions. The profiles of Fig. 4 correspond therefore to a planet where a mineralogical phase similar to that of the Earth's lower mantle is also present in the lighter shallow layers. These models have therefore a slightly larger density and pressure than PREM.

In Fig. 5, adiabatic profiles of density [using the approximation (14), bottom row] and temperature (top row) are depicted for different possible planets (gravity is assumed uniform, proportional to the thickness of the mantle and equal to Earth's value for a mantle thickness of 3000 km). We choose a surface top temperature T_t arbitrarily equal to $T_0 = 273$ K although in general, the reference temperature T_0 of the EoS and the surface temperature of the planet T_t are not identical (and are also different from the surface adiabatic temperature T_a^0). The situation for the Earth is roughly comparable to that depicted by the red curves. In the left-hand column, the mantle thickness H changes from

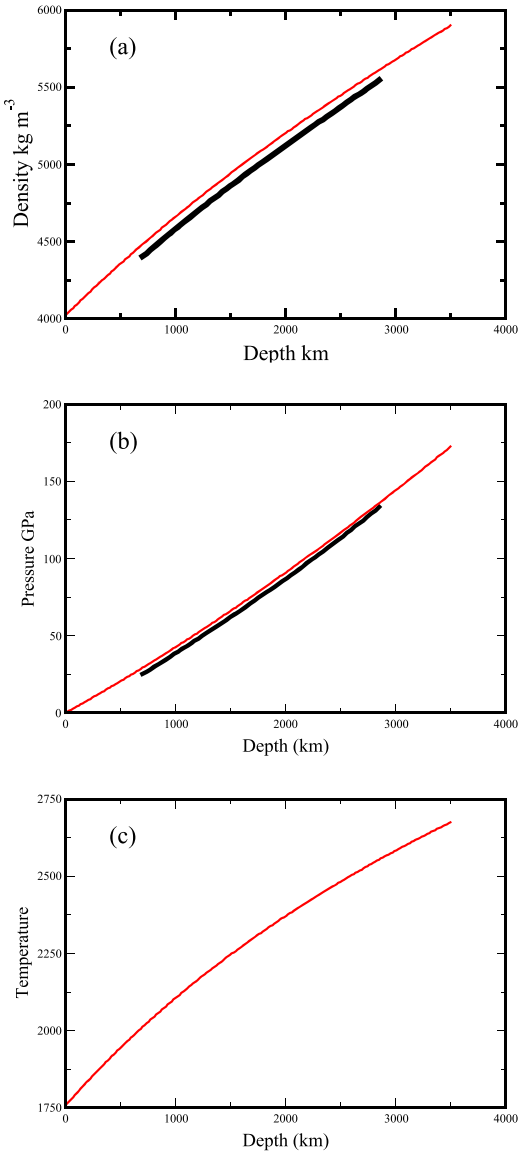

Figure 4. Adiabatic density (a), pressure (b) and temperature (c) as a function of depth using for the EoS the numerical values obtained by fitting the Earth lower mantle and assuming $C_P = C_V$. The density and pressure of PREM are shown in black. Since this model assumes a unique EoS for the upper and lower mantle, using values of Fig. 1 (red line) fitted to the lower mantle and disregarding the different phases of the upper mantle, the predictions have a higher density and consequently, a higher pressure than PREM.

2000 km (black), to 3000 km (red) and 4000 km (green) (and gravity increases from 6.5 to 9.8 and 13.1 m s^{-2}) and the bottom temperature T_b is kept fixed at 3000 K. All the geotherms (panel a) cross at mid-mantle by an arbitrary choice of the reference adiabatic temperature $[T_a(H/2) = (T_t + T_b)/2]$. The density increases with the mantle thickness (bottom left). In the right-hand column, the mantle thickness is constant (3000 km) and the bottom temperature is increased (2000, 3000 and 4000 K for black, red and green curves, respectively). Increasing the bottom temperature slightly decreases the densities. Note that all the different adiabatic profiles are very different from exponentials increasing with depth which are often assumed in numerical simulations using eqs (6a), (6b) and (6c) with constant α_a, g, Γ_0 and C_P (e.g. King *et al.* 2010).

Although the difference of C_P and C_V may not seem to have a major effect as we want to be as rigorous as possible we will account for their differences in our numerical methods. Furthermore the variations of the heat capacities with pressure and temperature are not negligible when global balance of energy is discussed. Assuming a uniform C_P would lead to the conclusion that the volume-averaged work done against gravity by the perturbed density exactly balances the volume-averaged viscous dissipation (Hewitt *et al.* 1975). This has been assumed true in many other papers although it is incorrect as pointed out by Alboussière & Ricard (2013). In the following, C_P will be computed from eq. (5) and the adiabatic density and temperature from eq. (6a) (assuming g uniform) and eq. (7).

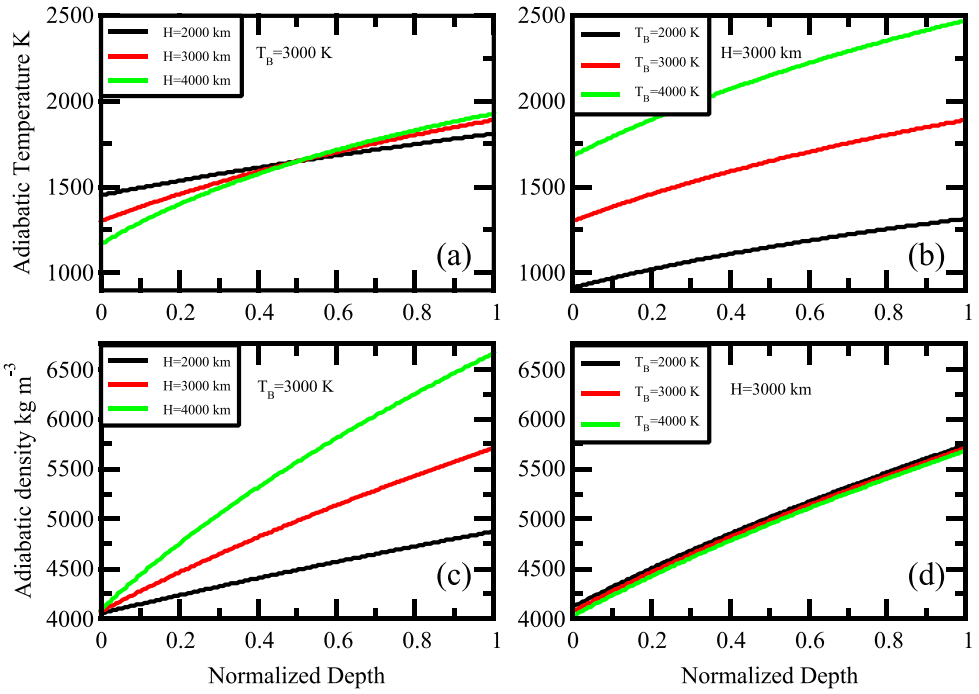

Figure 5. Possible density [using (14), bottom panels c and d] and temperature (top panels a and b) adiabatic profiles in various planets. In the left-hand column, the mantle thickness is increased with a constant bottom temperature. Gravity scales with the mantle thickness. In the right-hand column, the temperature is increased at constant mantle thickness. The Earth conditions are roughly similar to the intermediate case depicted in red.

Table 1. Scaling of the equations.

Quantity	Generic symbol	Scaling
Length	$x, z, h...$	H
Temperature	T	T_0
Density	ρ	ρ_0
Time	t	$\frac{H^2}{\kappa}$
Velocity	$\mathbf{u}$	$\frac{\kappa}{H}$
Thermal expansivity	α	α_0
Pressure or stress	P or τ	$\frac{\eta\kappa}{H^2}$
Heat capacity	C_V or C_P	C_V
Entropy	$\mathcal{S}$	C_V
Enthalpy	$\mathcal{H}$	$C_V T_0$

Table 2. Dimensionless numbers.

Name	Expression	Typical values	Values used in the paper
Grüneisen parameter	$\Gamma_0 = \frac{\alpha_0 K_T^0}{\rho_0 C_V}$	1–2	1
Dissipation number	$\mathcal{D} = \frac{\alpha_0 g H}{C_V}$	0.3–2	1
Thermal density variations	$\epsilon = \alpha_0 T_0$	10^{-3}–2×10^{-2}	10^{-2}
Top temperature	$\frac{T_t}{T_0}$	0.1–3	1
Bottom temperature	$r = \frac{T_b}{T_t}$	1–20	10
$\mathcal{R}$ number	$\mathcal{R} = \frac{\rho_0 g H^3}{\eta\kappa}$	10^3–10^{10}	10^5–10^9

2.5 Dimensionless EoS and reference profiles

In the next section, where we write the FC convection equations for a fluid obeying a Murnaghan EoS, we work with dimensionless quantities. We use the mantle thickness H, the surface temperature and density, T_0 and ρ_0 to define length, temperature and density units (see Table 1). We introduce several dimensionless numbers in addition to the Grüneisen parameter (see Table 2), among which the dissipation number $\mathcal{D} = \alpha_0 g H / C_V$ (note that our hypothesis of a constant C_V leads us to define $\mathcal{D}$ with C_V while classical papers rather use C_P), the thermal density factor $\epsilon = \alpha_0 T_0$ and a number $\mathcal{R} = \rho_0 g H^3 / \eta\kappa$ [the viscosity η and the thermal diffusivity $\kappa = k/(\rho_0 C_V)$ are used to scale the pressure

with $\eta\kappa/H^2$]. With the fit of the EoS using the PREM profile, we get $\mathcal{D} \approx 0.57$, $\epsilon \approx 6.7 \times 10^{-3}$, $\Gamma_0 \approx 1.22$. The introduction of the $\mathcal{R}$ number closely related to the Rayleigh number will become obvious when we will introduce the convection equations. With these units and definitions, the dimensionless EoS writes, from (9)

$$\rho = \left[1 + n\left(P\frac{\mathcal{D}}{\mathcal{R}\Gamma_0} - \epsilon(T-1)\right)\right]^{\frac{1}{n}} \tag{17}$$

or

$$P = \frac{\mathcal{R}\Gamma_0}{\mathcal{D}}\left(\frac{\rho^n - 1}{n} + \epsilon(T-1)\right), \tag{18}$$

and the adiabatic conditions (6a) and (6b) are

$$\frac{\mathrm{d}T_a}{\mathrm{d}z} = -\frac{\mathcal{D}T_a}{\rho_a^n \gamma_a}, \tag{19a}$$

$$\frac{\mathrm{d}\rho_a}{\mathrm{d}z} = -\frac{\mathcal{D}}{\Gamma_0 \gamma_a \rho_a^{n-2}}, \tag{19b}$$

where γ_a is C_P/C_V on the adiabat

$$\gamma_a = 1 + \Gamma_0 \epsilon \rho_a^{-n-1} T_a. \tag{20}$$

We emphasize that both C_P and C_V are necessary for a correct thermodynamic description: assuming a uniform C_P instead of a uniform C_V, and using C_P in the definition of the dissipation $\mathcal{D}$ would remove γ_a from (19a) to (19b), but it would reappear in the EoS [γ_a would divide the $\mathcal{D}/\mathcal{R}\Gamma_0$ factor present in (17)−(18)].

Before writing the entropy and enthalpy in dimensionless variables, we choose their integration constants. For the enthalpy, the constant $A_\mathcal{H}$ will never appear in our conclusions and can be taken equal to zero. For the entropy, we know that convection at high Rayleigh number leads to an isentropic mean state. We can choose the entropy to be zero along the adiabat (T_a, ρ_a). We have not yet explained how the surface adiabatic temperature T_a^0 which defines the temperature and density reference profiles is chosen but let us assume here that this choice is made. In that case, we therefore write in dimensionless form,

$$\mathcal{H} = \left(1 + \frac{\Gamma_0}{\rho}\right) T + \frac{\Gamma_0}{(n-1)\epsilon}\rho^{n-1}, \tag{21}$$

$$\mathcal{S} = \ln\frac{T}{T_a} + \Gamma_0\left(\frac{1}{\rho} - \frac{1}{\rho_a}\right). \tag{22}$$

In Table 2, we indicate the range of values that the dimensionless parameters can reach in planetary mantles. Note that $\mathcal{R}$ is different from the Rayleigh number which is classically defined in the Boussinesq case by $\mathrm{Ra} = \mathcal{R}\epsilon\Delta T$, where $\Delta T = T_b - T_t$ is the difference between the bottom and top temperatures, or in the compressible case by $\mathrm{Ra} = \mathcal{R}\epsilon(\Delta T - \Delta T_a)$, where ΔT_a is the adiabatic temperature jump across the layer. The vigour of convection in the simulations discussed in the next paragraphs corresponds to Rayleigh numbers Ra about 14 times smaller than $\mathcal{R}$ as we use $\epsilon \approx 10^{-2}$, $\Delta T - \Delta T_a \approx 7\,T_0$. With the FC equations and the EoS (17), using Ra instead of $\mathcal{R}$ would not have led to simpler expressions.

The dissipation number $\mathcal{D} = \alpha_0 g H/C_V$ is perhaps a quantity which might be less known to non-specialists. Of course, as α_0 and C_V are constants in our model, and mantle thickness and gravity roughly scale with the planetary radius, very large dissipation numbers could be obtained for massive exo-planets. However this might be misleading. One can argue that the compressible effects in convection are related to an average dissipation number

$$\langle\mathcal{D}\rangle = \frac{\langle\alpha\rangle g H}{C_V} \tag{23}$$

(assuming like for Earth's mantle, that g is mostly uniform and C_V constant). As α decreases with density (see (10b)) and therefore pressure, $\langle\alpha\rangle$ decreases with the size of the planet, the average dissipation number can never reach very large values. More precisely, using the expression of α, (14) and computing the density from (10b) assuming $h\propto 1/g \propto 1/H$ (see eq. 15), one can express $\langle\alpha\rangle$ and show that

$$\langle\mathcal{D}\rangle \leq \Gamma_0, \tag{24}$$

(we have assumed a uniform g but the fact that $\langle\mathcal{D}\rangle$ is bounded by a quantity that cannot be much larger than Γ_0 is also valid if g is linearly increasing with the radius). Although near the surface, the compressibility effects are very important and the dissipation number can be huge, the fact that the mantle becomes more and more incompressible as pressure increases (i.e. as g or H increases) makes the average dissipation at most of order of the Grüneisen parameter.

3 EQUATIONS OF COMPRESSIBLE CONVECTION UNDER DIFFERENT LEVELS OF SIMPLIFICATION

3.1 Starting set of equations of compressible convection

The FC equations of convection with infinite Prandtl number (no inertia) and uniform dynamic viscosity η, thermal conductivity k and gravity g, are in dimensional variables

$$\frac{\mathrm{D}\rho}{\mathrm{D}t} + \rho\nabla\cdot\mathbf{u} = 0, \tag{25a}$$

$$\eta\nabla^2\mathbf{u} + \frac{\eta}{3}\nabla\nabla\cdot\mathbf{u} - \nabla P + \rho\mathbf{g} = 0, \tag{25b}$$

$$\rho T\frac{\mathrm{D}\mathcal{S}}{\mathrm{D}t} = \dot{\varepsilon} : \tau + \nabla^2 T, \tag{25c}$$

where $\mathbf{u}$ is the velocity, $\dot{\varepsilon}_{ij} = 1/2(\partial_j u_i + \partial_i u_j)$ is the strain rate tensor and $\tau_{ij} = 2\eta\dot{\varepsilon}_{ij} - (2/3)\eta\,\delta_{ij}\nabla\cdot\mathbf{u}$ the stress tensor with zero bulk viscosity. In addition to the quantities already discussed (see Table 1), we non-dimensionalize time and velocities with H^2/κ and κ/H. Finally, using the chosen EoS and the entropy expression (13a), we get, without dimensions,

$$\frac{\mathrm{D}\rho}{\mathrm{D}t} + \rho\nabla\cdot\mathbf{u} = 0, \tag{26a}$$

$$\nabla^2\mathbf{u} + \frac{1}{3}\nabla\nabla\cdot\mathbf{u} - \nabla P - \mathcal{R}\rho\mathbf{e}_z = 0, \tag{26b}$$

$$\rho\frac{\mathrm{D}T}{\mathrm{D}t} + \Gamma_0 T\nabla\cdot\mathbf{u} = \frac{\mathcal{D}}{\mathcal{R}\epsilon}\dot{\varepsilon} : \tau + \nabla^2 T. \tag{26c}$$

This system is supplemented by the EoS, that is, by the pressure definition (18). Finally, the non-dimensional top and bottom temperatures must be defined. We choose indeed to define their ratio $r = T_b/T_t$, and the top dimensionless temperature T_t/T_0.

3.2 Derivation of FC equations in terms of density and temperature variables

Let us replace all variables X by $X_a + X'$ where X_a are the values on the adiabatic profiles, and the new variables X' are now the differences with the adiabatic case. However contrary to the usual AA we do not assume that the X' are necessarily small. As we have a differential system with time evolution equations for density and temperature, we also use the EoS to express the pressure and write the whole system in ρ'–T' variables, with w being the velocity component against gravity:

$$\frac{\mathrm{D}\rho'}{\mathrm{D}t} + \rho_a\nabla\cdot\mathbf{u} + w\frac{\mathrm{d}\rho_a}{\mathrm{d}z} + \rho'\nabla\cdot\mathbf{u} = 0, \tag{27a}$$

$$\nabla^2\mathbf{u} + \frac{1}{3}\nabla\nabla\cdot\mathbf{u} - \frac{\mathcal{R}\Gamma_0}{\mathcal{D}}\left[(\rho_a+\rho')^{n-1}\nabla\rho' + \epsilon\nabla T'\right] - \left\{\frac{\mathcal{R}\Gamma_0}{\mathcal{D}}\left[(\rho_a+\rho')^{n-1} - \rho_a^{n-1}\right]\frac{\mathrm{d}\rho_a}{\mathrm{d}z} + \mathcal{R}\rho'\right\}\mathbf{e}_3 = 0, \tag{27b}$$

$$(\rho_a+\rho')\frac{\mathrm{D}T'}{\mathrm{D}t} + w\rho_a\frac{\mathrm{d}T_a}{\mathrm{d}z} + w\rho'\frac{\mathrm{d}T_a}{\mathrm{d}z} + \Gamma_0(T_a+T')\nabla\cdot\mathbf{u} = \frac{\mathcal{D}}{\mathcal{R}\epsilon}\dot{\varepsilon} : \tau + \nabla^2(T_a+T'). \tag{27c}$$

As we later solve the system of equations with the software Dedalus (Burns *et al.* 2020), which handles differential equations of the form

$$M\frac{\partial X}{\partial t} + LX = F, \tag{28}$$

where the matrices M and L must be linear on the problem variables, all non-linear quantities above are written as the sum of their first order expansion that will be accounted for by the matrices M and L, and a non-linear correction that will be accounted for by F. For example in the term containing the density gradient of (27b), we use

$$(\rho_a+\rho')^{n-1}\nabla\rho' = \rho_a^{n-1}\nabla\rho' + \left((\rho_a+\rho')^{n-1} - \rho_a^{n-1}\right)\nabla\rho', \tag{29}$$

the first term of the right-hand side being linear in ρ' is included in L, the second, non-linear, is included in F (the first term of its Taylor expansion is $(1/2)(n-1)\rho_a^{n-2}\nabla\rho'^2$). We also define the scale height of the adiabatic density change, m, which is depth-dependent

$$m = \frac{1}{\rho_a}\frac{\mathrm{d}\rho_a}{\mathrm{d}z} = -\frac{\mathcal{D}}{\Gamma_0\gamma_a\rho_a^{n-1}}. \tag{30}$$

With this method and definition, the left-hand side (LHS) of the convection eqs (27a)–(27c) becomes

$$\partial_t \rho' + \rho_a(\boldsymbol{\nabla}\cdot\mathbf{u} + mw) = F_1, \tag{31a}$$

$$\nabla^2 u + \frac{1}{3}\partial_x \boldsymbol{\nabla}\cdot\mathbf{u} - \frac{\mathcal{R}\Gamma_0}{\mathcal{D}}\left(\rho_a^{n-1}\partial_x\rho' + \epsilon\partial_x T'\right) = F_2, \tag{31b}$$

$$\nabla^2 w + \frac{1}{3}\partial_z \boldsymbol{\nabla}\cdot\mathbf{u} - \frac{\mathcal{R}\Gamma_0}{\mathcal{D}}\left(\rho_a^{n-1}\partial_z\rho' + \epsilon\partial_z T'\right) - \mathcal{R}\rho'\left(1 - \frac{n-1}{\gamma_a}\right) = F_3, \tag{31c}$$

$$\partial_t T' - \frac{\nabla^2 T'}{\rho_a} = F_4, \tag{31d}$$

with the right-hand side (RHS) terms

$$F_1 = -\boldsymbol{\nabla}\cdot(\rho'\mathbf{u}), \tag{32a}$$

$$F_2 = \tfrac{\mathcal{R}\Gamma_0}{\mathcal{D}}\left[(\rho_a+\rho')^{n-1} - \rho_a^{n-1}\right]\partial_x\rho', \tag{32b}$$

$$F_3 = \frac{\mathcal{R}\Gamma_0}{\mathcal{D}}\left[(\rho_a+\rho')^{n-1} - \rho_a^{n-1}\right]\partial_z\rho' + \frac{\mathcal{R}\Gamma_0}{\mathcal{D}}\left[(\rho_a+\rho')^{n-1} - \rho_a^{n-1} - (n-1)\rho_a^{n-2}\rho'\right]\mathrm{d}_z\rho_a, \tag{32c}$$

$$F_4 = -\mathbf{u}\cdot\boldsymbol{\nabla}T' - \frac{mw\Gamma_0}{\rho_a}\frac{\rho' T_a - \rho_a T'}{\rho_a+\rho'} - \Gamma_0\frac{T_a+T'}{\rho_a+\rho'}(\boldsymbol{\nabla}\cdot\mathbf{u} + mw) + \frac{\mathcal{D}}{\mathcal{R}\epsilon}\frac{\dot{\varepsilon}:\tau}{\rho_a+\rho'} - \frac{\rho'}{\rho_a}\frac{\nabla^2 T'}{\rho_a+\rho'} + \frac{1}{\rho_a+\rho'}\mathrm{d}_{zz}^2 T_a. \tag{32d}$$

The diffusion $\mathrm{d}_{zz}^2 T_a$ along the adiabat can be expressed analytically using (19a) and (19b)

$$\mathrm{d}_{zz}^2 T_a = \frac{\mathcal{D}^2 T_a}{\gamma_a^2\rho_a^{2n}}\left(1 - n\frac{\rho_a}{\Gamma_0}\right) - \frac{\mathcal{D}^2 T_a^2\epsilon\Gamma_0}{\gamma_a^3\rho_a^{3n+1}}\left(1 - (n+1)\frac{\rho_a}{\Gamma_0}\right). \tag{33}$$

This writing allows us to easily identify the usual anelastic terms (Ogura & Phillips 1962; Jarvis & McKenzie 1980; Braginsky & Roberts 1995; Lantz & Fan 1999) and the additional terms necessary for the FC set of equations.

3.3 Notes on various AAs in literature

The AA has been mostly introduced to avoid the propagation of sound waves in a convective medium, that would lead to impractically small time steps in numerical models to be properly solved. The approximation was made in situations with large Reynolds numbers such as the atmosphere (Ogura & Phillips 1962), the liquid core (Braginsky & Roberts 1995) or the stars (Lantz & Fan 1999). It starts with removing the $\partial\rho'/\partial t'$ from the mass conservation. However the situation is very different in mantle convection with infinite Prandtl number, where the generation of sound waves is already impossible by the absence of inertia in the Stokes equation [see e.g. Schubert *et al.* (2001); Ricard (2015) for a discussion focused on planetary mantle, or Curbelo *et al.* (2019)]. Once $\partial\rho'/\partial t'$ is removed, mass conservation becomes $\boldsymbol{\nabla}\cdot(\rho\mathbf{u}) = 0$ which is implemented as $\boldsymbol{\nabla}\cdot(\rho_a\mathbf{u}) = 0$. The AA then proceeds by using the first order expansion of the EoS, which in our case would be

$$\rho' = \frac{1}{\rho_a^{n-1}}\left(\frac{\mathcal{D}}{\mathcal{R}\Gamma_0}P' - \epsilon T'\right) \tag{34}$$

and by considering that all prime variables are small perturbations around the adiabatic profiles.

The first order expression of the entropy time derivative (25c) is $\rho_a T_a \mathrm{D}\mathcal{S}'/\mathrm{D}t$ as $\mathcal{S}_a$ is constant along the adiabatic profile [and is even zero according to eq. (22)]. However, from this point on, several paths have been followed in expressing $\mathcal{S}'$ as a function of any couple of variables among T', P' or ρ' (most previous papers are also written using temperature and pressure variables, T', P' contrary to our approach using T', ρ'). In particular the approximations on the constancy or the variability of the various parameters, C_V, C_P, α, K_T, Γ... are rarely discussed and sometimes inadvertently made.

Earlier authors use both $\alpha T = 1$ (which would be valid for an ideal gas) and constant α and C_P (Jarvis & McKenzie 1980; Machetel & Yuen 1989; Solheim & Peltier 1990). In the classic book on mantle convection (Schubert *et al.* 2001), $\mathcal{S}'$ is effectively replaced by $C_P T'/T_a$ which constitutes the anelastic liquid approximation (ALA) where the entropy is only related to temperature (see also Curbelo *et al.* 2019). Schubert *et al.* (2001) also uses constant and identical heat capacities. This ALA approximation leads to

$$\rho_a T_a\frac{\mathrm{D}\mathcal{S}'}{\mathrm{D}t} = \rho_a C_P\frac{\mathrm{D}T'}{\mathrm{D}t} - \rho_a C_P\frac{T'}{T_a}w\frac{\partial T_a}{\partial z} = \rho_a C_P\frac{\mathrm{D}T'}{\mathrm{D}t} + \rho_a\alpha_a g w T'. \tag{35}$$

The expression (35) has been implemented in many subsequent codes used in solid Earth geophysics to solve the heat equation in the AA formalism [in addition to the conduction and dissipation terms of (25c), e.g. Tackley 2008; King *et al.* 2010]. With our EoS, the term $\rho_a\alpha_a g w T'$ of the previous equation writes $\mathcal{D}wT'/\gamma_a\rho_a^{n-1}$ in dimensionless quantities.

Note that although C_P does not vary much, the contribution of its variations to the entropy changes is not totally negligible. With the Murnaghan EoS, and neglecting the pressure dependence of entropy (ALA) like in Schubert *et al.* (2001), the term

$$\rho_a T' \frac{\mathrm{D}C_P}{\mathrm{D}t} = \rho_a T' C_V w \frac{\partial(\Gamma_a \alpha_a T_a)}{\partial z} \tag{36}$$

should be added to (35). After non-dimensionalisation, this omitted term amounts to $-(\Gamma_0 \epsilon T_a/\rho_a^{n+1})(1-(n+1)\rho_a/\Gamma_0)$ times the term which has been included, $\mathcal{D}wT'/\gamma_a\rho_a^{n-1}$. The scale of temperature variation ϵ is indeed small, $\approx 2\times 10^{-2}$, but with $n\approx 3-4$, $T_a \approx 5$ and $\Gamma_0 \approx 1$, the term that has been neglected is about 30 per cent of the term kept in (35). Both C_P and C_V appear in the equations so that considering C_P as a constant as was previously done, would not make the problem disappear as C_V would then be variable. Although $\gamma_a = C_P/C_V \approx 1$, its depth derivative appears in the energy equation and does not vary much less than the derivatives of ρ_a or of T_a.

Bercovici *et al.* (1992) keep the pressure dependence of the entropy (i.e. use $\mathcal{S}' = C_P T'/T_a - \alpha_a P'/\rho_a$) but they also consider constant thermodynamics parameters (C_P, α, etc.). In the astrophysical literature, the researchers work directly in term of entropy (e.g. Currie & Browning 2017) which removes some problems but replaces the diffusion of temperature by a diffusion of entropy which is another approximation (Lecoanet *et al.* 2014). Of course the high Reynolds number and ideal gas of astrophysics simulations make the applicability of their approximations remote from the mantle situation.

In the solid Earth community, other approximations are sometimes made with the AA Stokes equation like removing the pressure dependence of density in the truncated anelastic liquid approximation TALA (see e.g. Tan & Gurnis 2007) or keeping $\boldsymbol{\nabla}\cdot\mathbf{u}=0$ as a mass conservation equation [which is sometimes called extended Boussinesq approximation (EBA), see King *et al.* (2010) for an overall discussion]. They systematically lead to thermodynamic inconsistencies (see e.g. Leng & Zhong 2008). We think that these are suppressed by our approach where all variables are rigorously defined from the EoS.

3.4 Proposed equations of AA convection

In this section we write our own version of the AA equation, since we do not want to identify C_V and C_P and since we use $\rho'-T'$ variables instead of the more common P'–T' variables. We start in agreement with earlier attempts, by replacing the mass conservation by

$$\boldsymbol{\nabla}\cdot(\rho_a\mathbf{u}) = \rho_a(\boldsymbol{\nabla}\cdot\mathbf{u} + mw) = 0 \tag{37}$$

and we express the momentum equations at first order (e.g. Schubert *et al.* 2001). This simply means cancelling the RHS terms F_2 and F_3 of the FC Stokes equation.

More attention is deserved for the heat eq. (27c) with a RHS containing six terms in FC expression (32d). We obviously keep the first advection term. We can remove the ρ' from the denominator of the 2nd, 3rd, 4th and 6th terms (associated with 2nd order effects) and neglect the 5th term (already 2nd order). In the 3rd term we should not remove the $\boldsymbol{\nabla}\cdot\mathbf{u}+mw$ term on the argument that we use $\boldsymbol{\nabla}\cdot(\rho_a\mathbf{u}) = \rho_a(\boldsymbol{\nabla}\cdot\mathbf{u}+mw)=0$ as a proxy for mass conservation. Thermodynamics rules cannot be true unless P, T and ρ are exactly related by the EoS. The $\boldsymbol{\nabla}\cdot\mathbf{u}+mw$ in (32d) must be replaced by its true value according to (31a), that is $\boldsymbol{\nabla}\cdot\mathbf{u}+mw = -(\partial\rho'/\partial t + \boldsymbol{\nabla}\cdot(\rho'\mathbf{u}))/\rho_a$, which is a first-order term, otherwise various basic thermodynamic equalities become wrong. For example, thermodynamics requires that the exchanges of heat verify

$$C_V\frac{\mathrm{D}T}{\mathrm{D}t} - \frac{\alpha K_T}{\rho^2}\frac{\mathrm{D}\rho}{\mathrm{D}t} = C_P\frac{\mathrm{D}T}{\mathrm{D}t} - \alpha T\frac{\mathrm{D}P}{\mathrm{D}t}, \tag{38}$$

and this equality will not be verified if $\mathrm{D}\rho/\mathrm{D}t = -\rho\boldsymbol{\nabla}\cdot\mathbf{u}$ is replaced by ρmw.

To sum up, in addition to the approximate mass conservation (37), the RHS of the other eqs (32) becomes in the anelastic formulation

$$F_2 = 0, \tag{39a}$$

$$F_3 = 0, \tag{39b}$$

$$F_4 = -\mathbf{u}\cdot\boldsymbol{\nabla}T' - \frac{\Gamma_0 mw}{\rho_a^2}(\rho' T_a - \rho_a T') + \Gamma_0\frac{T_a}{\rho_a^2}\left(\frac{\partial\rho'}{\partial t} + \boldsymbol{\nabla}\cdot(\rho'\mathbf{u})\right) + \frac{1}{\rho_a}\frac{\mathcal{D}}{\mathcal{R}\epsilon}\dot{\varepsilon}:\tau + \frac{\mathrm{d}^2_{zz}T_a}{\rho_a}, \tag{39c}$$

(the $\partial\rho'/\partial t$ term can also be moved to the LHS). Note that the ALA approximation with constant C_P would make the F_4 term equal to

$$F_4^0 = -\mathbf{u}\cdot\boldsymbol{\nabla}T' + \frac{\Gamma_0 mw}{\rho_a}T' + \frac{1}{\rho_a}\frac{\mathcal{D}}{\mathcal{R}\epsilon}\dot{\varepsilon}:\tau + \frac{\mathrm{d}^2_{zz}T_a}{\rho_a}. \tag{40}$$

We will use this expression in one of our simulations.

3.5 The quasi-Boussinesq (QB) equations

The BA consists in using $\mathcal{D} = 0$ in the AA equations. This cancels all depth dependence for the adiabatic profiles. Assuming that the background density is uniform implicitly implies that $\rho^{'}/\rho_a$ is also neglected. However this does not prohibit the assumption that the thermal expansivity in the Stokes equation is depth dependent (see e.g. Schmeling *et al.* 2003) [the thermal diffusivity could also be depth dependent as in Dubuffet *et al.* (1999)]. We call this a QB model as the strict Boussinesq model is with a constant thermal expansivity. In the solid Earth community, it is common, as a first order estimate, to run Boussinesq or QB models to get a temperature model on which the adiabatic gradient is added *a posteriori*. This clearly challenges the rules of thermodynamics. However we think it may be useful to add this QB approach to the AA and FC models, in which case we solve

$$\boldsymbol{\nabla} \cdot \mathbf{u} = 0, \tag{41a}$$

$$\boldsymbol{\nabla}^2 \mathbf{u} - \boldsymbol{\nabla} P - \frac{\mathcal{R}\epsilon}{\rho_a^{n-1}} T \mathbf{e}_z = 0 \tag{41b}$$

$$\frac{\mathrm{D}T}{\mathrm{D}t} - \nabla^2 T = 0. \tag{41c}$$

In this equation set based on shaky foundations we have implicitly considered that the background density is ρ_0 but used $\rho' = -\rho_a \alpha_a T = -T/\rho_a^{n-1}$ in (41b) (i.e. $\alpha \propto \rho_a^{1-n}$). One might argue that the Boussinesq model with variable expansivity mimicking a compressible convection should rather consider a background density related to the average of ρ_a and should use $\rho' = -\alpha_a T = -T/\rho_a^n$ (i.e. $\alpha \propto \rho_a^{-n}$). This alternate choice and our own choice are truly arbitrary as there is indeed no rigorous way to simulate compressible convection with a QB formalism.

3.6 Boundary conditions

We will use the previous FC, AA and QB systems of equations to perform numerical simulations of convection in a 2-D fixed volume. The horizontal variable is x and the flow is assumed periodic in a box of aspect ratio 4. In the FC and AA cases, the $T^{'}$ temperature (i.e. the total temperature minus the adiabat) is imposed on top, $T^{'}(1) = 1 - T_a(1)$, and at the bottom, $T^{'}(0) = r - T_a(0)$, where r is the dimensionless bottom temperature (see Table 2). In the QB case, the temperature difference is the same non-adiabatic quantity $\Delta T_{\mathrm{na}} = r - 1 - [T_a(0) - T_a(1)]$.

In the QB case, the other boundary conditions usually adopted for mantle convection are free slip boundary conditions on top and bottom. To avoid a global horizontal translation of the system that constitutes a trivial solution, a zero average horizontal velocity at the top can also be imposed. In the QB case, only the pressure gradient appears in the equations and, for example, the average pressure value at the surface can be chosen if the pressure field is needed. These boundary conditions are implemented in our incompressible QB cases.

For the FC and AA cases, these conditions are unfortunately incompatible with the compressible nature of the fluid when the simulations are performed in a fixed volume. The total mass M of the convective layer

$$M = \int (\rho_a + \rho') \, \mathrm{d}V, \tag{42}$$

can indeed be chosen arbitrarily and that choice affects the final pressure needed to squeeze or expand this mass into the convecting volume. The EoS depending of the pressure, we should also monitor the surface pressure so that its time averaged value is reasonable. For instance, applying our model to the Earth, we would like the surface pressure to be close to zero (or 1 atm) and not, say, close to 20 GPa which would be the pressure in the transition zone. The mass M should therefore be chosen so that it ultimately leads to the correct surface pressure. However without running the convection code until statistical steady state we have no possibility to know the surface pressure. Of course this problem arises from using a fixed volume. In a simulation using a deformable volume, the thickness of the convective layer would increase or decrease to contain the mass introduced in the simulation and the difficulty would be to choose the initial mass such that the final mantle thickness is reasonably close to H.

In the FC case, the conservative nature of the mass conservation eq. (26a), ensures that the total mass is conserved. We can therefore start our FC simulations with a uniform $\rho^{'} = 0$ so that the total mass remains that computed from the adiabatic density, that is

$$M = \int \rho_a \, \mathrm{d}V. \tag{43}$$

This mass is in fact directly related to the surface adiabatic density or adiabatic temperature which is chosen (and even directly proportional to the surface adiabatic density according to the approximated eq. (14)). The problem is therefore to choose the correct appropriate surface adiabatic temperature (the foot of the adiabatic), so that the statistical steady-state surface pressure $\overline{P_a + P'}(1) = \overline{P'}(1)$ is zero (or another chosen value) and the surface density $\overline{\rho_a + \rho'}(1)$ is ρ_0 (overlined quantities represent statistically steady state quantities, averaged in time and horizontally). Note that the instantaneous average surface pressure (and furthermore the instantaneous local normal stress at the surface) is not necessarily zero and this is usually interpreted as equivalent to a weak dynamic topography forced by the internal convection (e.g. Ricard *et al.* 2014).

Our strategy for the FC case, is therefore the following:

(i) We start from an adiabatic temperature profile such that the temperature at mid depth is $T_a^{1/2} = (1 + r)/2 + \beta$, where β is initially zero.

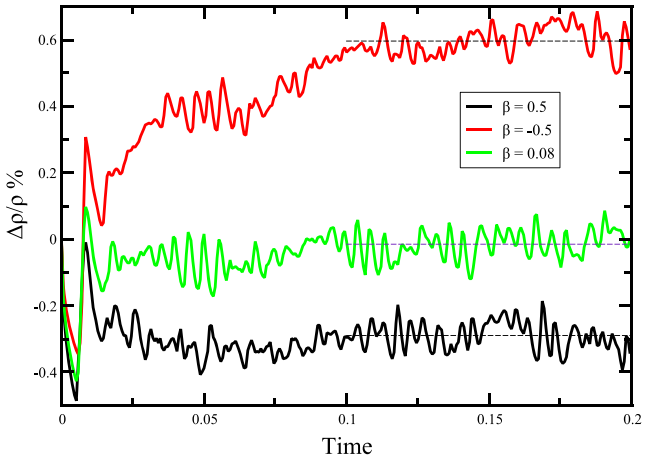

Figure 6. The average surface density in a FC convection model with $\mathcal{R} = 10^7$ (in percent with respect to ρ_0) is computed as a function of time for various *a priori* adiabatic profiles with $\beta = -0.5$, 0.5 and 0.08 (red, black, and green line, respectively). For $\beta = 0.08$, a surface density close to ρ_0 is obtained. To estimate the correct adiabatic profile, we perform two simulations (i.e. for $\beta = -0.5$, 0.5), compute the average surface density when a steady state situation is reached (thin dotted lines) and correct the adiabat by linear interpolation.

(ii) We run the convection code using the corresponding adiabatic density and temperature profiles and compute the surface pressure $\overline{P'}(1)$ at stationary steady state

(iii) If $\overline{P'}(1) \neq 0$, we modify the adiabatic profile by shifting the adiabatic temperature by β (see also Curbelo *et al.* 2019).

(iv) We run again the convection code with the new adiabatic profile until $\overline{P'}(1) = 0$.

This strategy is not numerically too heavy: the relation between $\overline{P'}(1)$ and β appears to be quasi-linear; when simulations with two different β are performed, the two computed surface densities are generally enough to guess by interpolation the correct temperature shift that leads closely to an average zero pressure at the surface. We illustrate our method in Fig. 6. Convection simulations have been computed for $\mathcal{R} = 10^7$ and the values $\beta = 0.5$ (black) and –0.5 (red). We plot the relative difference in per cent of the average surface density $(\overline{\rho}(1) - \rho_0)/\rho_0 \approx \overline{P}(1)\mathcal{D}/\mathcal{R}\Gamma_0$, (see eq. 17). When the adiabatic profile is too cold (red curve), a too large mass is assumed in the convecting box implying a surface excess pressure and a density larger than the assumed surface density ρ_0 by ≈0.6 per cent. By contrast a too hot adiabatic profile (black) would lead to a ≈0.3 per cent too light surface density. By interpolation, we guess that the appropriate adiabatic temperature reaches at mid depth the temperature $T_a^{1/2} = (1 + r)/2 + \beta$, where $\beta \approx 0.08$ (green line). Shifting the adiabatic profile from –0.5 to 0.5 changes the surface density and the statistically steady state density profile by around 1 per cent and the steady state temperature profiles by around 3 per cent. This value of $\beta \approx 0.08$ seems to bring the surface pressure close to zero for all $\mathcal{R}$ numbers. In other words the adiabatic temperature at mid-depth is slightly larger than the average of the top and bottom temperatures.

The adiabatic profiles selected for the FC case are also used for the corresponding AA simulations. However the anelastic mass conservation (37) does not imply

$$\int \rho' \, \mathrm{d}V = \text{Constant} \tag{44}$$

and therefore does not imply that the total mass is conserved (see eq. 42). Surprisingly we have not found in the literature an indication on how the various compressible codes that have been used and benchmarked (e.g. in King *et al.* 2010) have kept the total mass of their convective volume constant. Here we enforce mass conservation by imposing the average values of P' on the top and bottom boundaries to be equal. The Stokes equation integrated over the total volume when horizontal periodic conditions are imposed (see Alboussière *et al.* 2022), implies indeed that

$$\int \left[P'(x, 1, t) - P'(x, 0, t)\right] \mathrm{d}x = 0 \Rightarrow \int \rho' \, \mathrm{d}V = 0. \tag{45}$$

To summarize, all our simulations use free slip boundary conditions on top and bottom. The time-average surface pressure is exactly zero (QB case) or very close to zero (FC case). This is obtained by choosing the appropriate surface adiabatic temperature (which is equivalent to choosing the total mass in the convective layer). The same adiabatic profile is used in the AA case where mass conservation is enforced by (45).

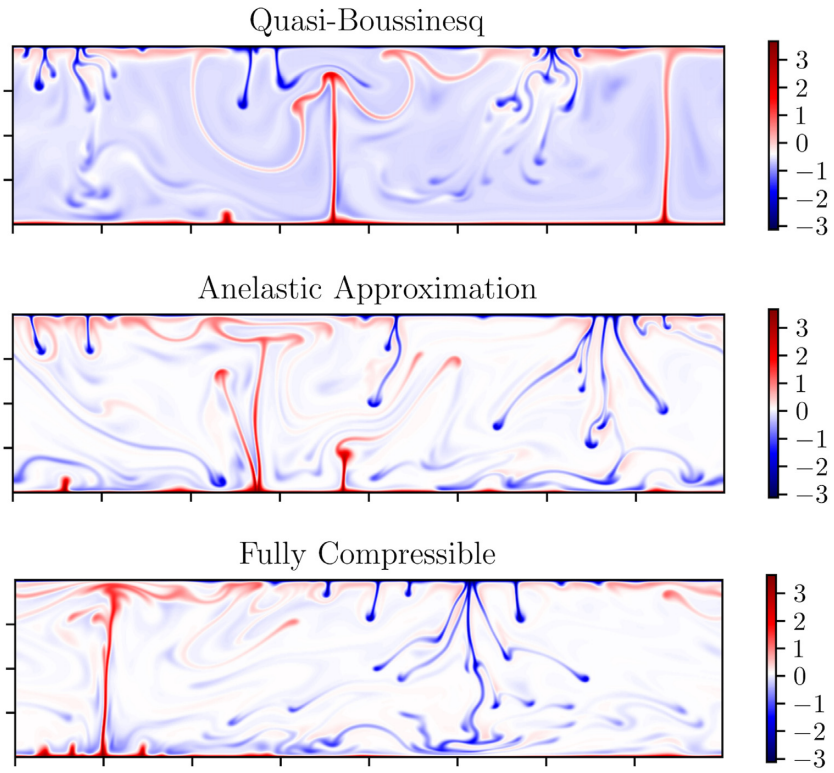

Figure 7. Snapshots of the non-adiabatic temperature field at $\mathcal{R} = 10^9$ using the QB, AA and FC approximations. The temperature colour scales are slightly different in the three cases but over the same imposed non-adiabatic range. The QB temperature is clearly lower than in both other cases.

4 NUMERICAL SIMULATIONS

4.1 Numerical setup

We can now perform various simulations to compare the approximated simulations (QB and AA) to the FC case. The simulations are performed in a domain of aspect ratio 4. The Dedalus software is used (Burns *et al.* 2020, www.dedalus-project.org), whose resolution is based on Fourier Transform for the horizontal direction and Chebyshev polynomials for the vertical direction. We choose the number of points so that the top and bottom thermal boundary layers are described by at least 10 Chebyshev collocation nodes by using from 64×256 to 256×1024 nodes. The variables are advanced in time by a Runge–Kutta scheme of four-stage and order 3 (RK443, Ascher *et al.* 1997). Dedalus uses MPI and we distribute the computation so that each computer node handles 8–10 rows of our computation grid. The duration of a numerical run is around three to four times larger for FC than for QB. The AA simulation is somewhat in between (two times larger than for QB) and we have not tried to optimize the code which computes and records more ancillary quantities than needed. All the simulations are performed by varying $\mathcal{R}$ from 10^5 to 10^9 and keeping constant the values $\mathcal{D} = 1$, $\epsilon = 10^{-2}$, $\Gamma_0 = 1$, $n = 3.3$ and $r = 10$ which are in the range of parameters expected for the Earth mantle (see Table 2; as $T_t = 273$ K, the bottom temperature is $T_b = 2730$ K).

4.2 Examples of temperature fields

The subject of this paper will mostly be on the differences between the statistical steady-state and depth-dependent average quantities in the different approximations. However Fig. 7 depicts snapshots of QB, AA and FC simulations for $\mathcal{R} = 10^9$. The maps have characteristics that are shared with previous publications. The decrease of thermal expansivity with depth tends to broaden the thermal structures at depth (Hansen *et al.* 1993). As the hot instabilities gain buoyancy as they rise in the mantle (i.e. $\alpha_a \rho_a$ increases with height), they are stronger and more stationary than the cold instabilities that lose buoyancy with depth. This is particularly visible in the QB computation where the decrease of thermal expansivity is the only addition to the well-known and up-down symmetric Boussinesq case. The AA and FC simulations are richer in short wavelengths than the QB simulations. They also predict a larger average temperature of the bulk as will be discussed below. The larger average temperature in the AA and FC cases, by decreasing the buoyancy of hot plumes and increasing that of cold plumes, reinforces the downwellings (this mitigates the effect of expansivity predicted from QB models). Visually and qualitatively the characteristics of convection in the AA and FC cases look very similar.

Various quantities could be compared between the different simulations but we will focus here on the average profiles of temperature, pressure, heat flow and dissipation. When the differences between the QB, AA and FC profiles are small, we plot the FC profiles and the

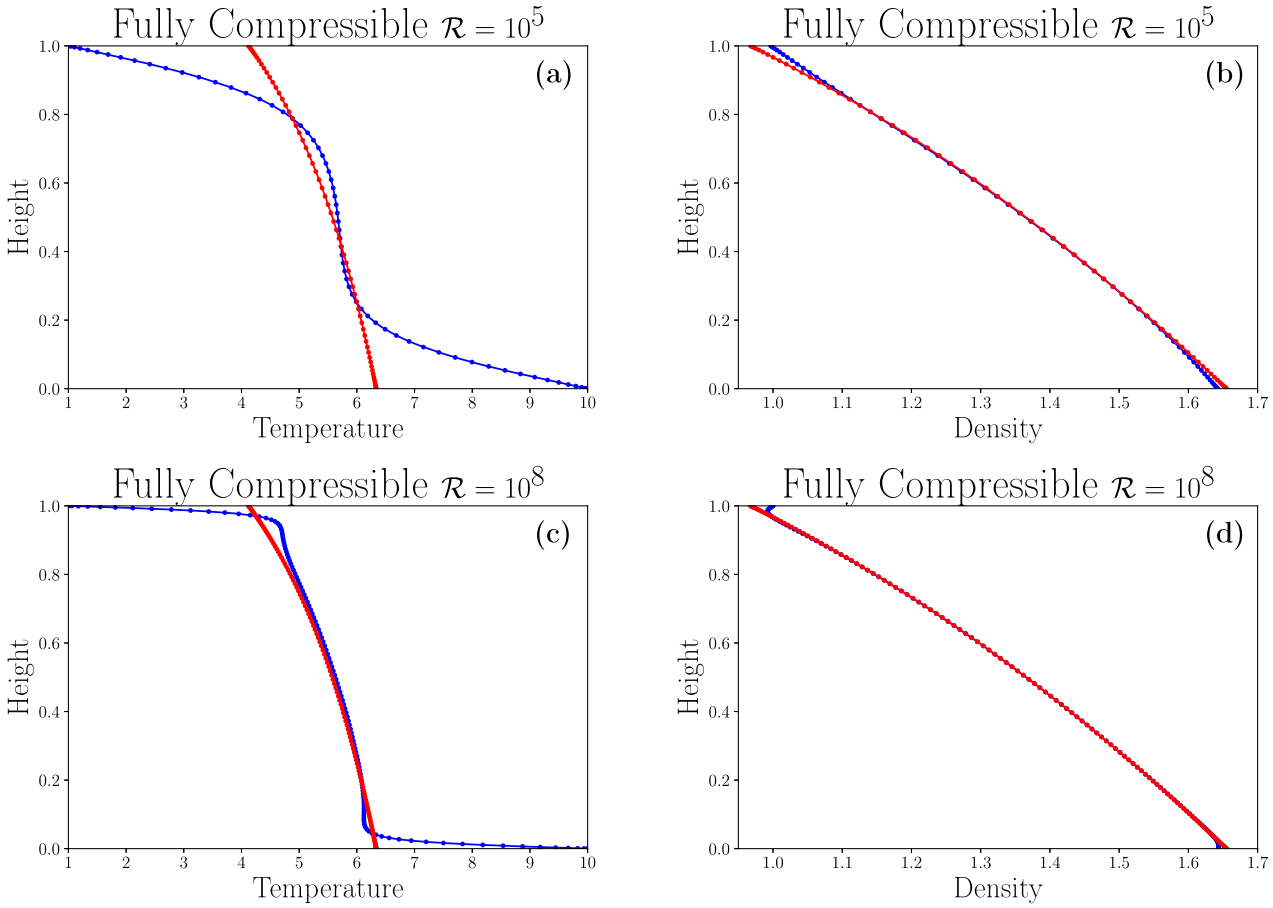

Figure 8. Mean temperature (left-hand column, a and c) and density (right-hand column, b and d) profiles across the convective layer (blue lines). The red lines correspond to the adiabatic approximation. The dots indicate the vertical positions of the collocation points. Top row (a and b) are for $\mathcal{R} = 10^5$, bottom row (c and d) for $\mathcal{R} = 10^8$.

differences between the approximated profiles and the FC ones. In addition to the figures discussed in the core of this paper, a complete set of figures is available in the supplementary material, from $\mathcal{R} = 10^5$ to $\mathcal{R} = 10^9$.

4.3 Temperature and density profiles

Fig. 8 depicts in blue the temperature (left-hand columns, panels a and c) and density profiles (right-hand columns, panels b and d) for the FC simulations for $\mathcal{R} = 10^5$ (top row, panels a and b) and $\mathcal{R} = 10^8$ (bottom row, panels c and d). The adiabatic profiles are shown in red. The red and blue dots indicate the vertical position of the Chebyshev collocation points. The total temperature drop $\Delta T = r - 1$ is 9. The adiabatic temperature drop is 2.21 reducing the driving temperature difference to $\Delta T_{\rm na} = 6.79$. The classical Rayleigh numbers $\mathrm{Ra} = \mathcal{R}\epsilon\Delta T_{na}$ are therefore $\mathrm{Ra} \approx 7 \times 10^3$ and $\mathrm{Ra} \approx 7 \times 10^6$.

The temperature is still far from adiabatic when $\mathcal{R} = 10^5$ (panel a) but very close to it at $\mathcal{R} = 10^8$ (panel c). Increasing the vigour of convection brings the bulk of the fluid closer to an isentropic state and the anelastic formalism becomes a better approximation of the FC case. We do not have a clear explanation of this observation that may be related to the specific EoS that we use. Indeed, although increasing the $\mathcal{R}$ number and the fluid velocity brings each individual parcel of the fluid in a state closer to adiabaticity, the amplitude of the temperature variations remains constant. Therefore the difference of the local temperature to the average adiabatic temperature (assumed small in the AA approximation) should not decrease much with $\mathcal{R}$. The density profiles (panels b and d) closely follow the adiabatic estimates except in the two thermal boundary layers. The decrease of the thermal expansion coefficient with depth makes the boundary layers asymmetrical in terms of densities with a top cold boundary layer more conspicuous than the bottom boundary layer (see panel d). The pressure profiles obtained from the convection simulation (not shown) are basically indistinguishable from the adiabatic predictions even in the boundary layers.

The differences between the profiles are more visible in Figs 9 and 10 computed with a $\mathcal{R}$ number of 10^5 and 10^8, respectively. The adiabatic profiles have been subtracted from the computed ones on the left-hand column, with the FC profile in red, the AA and QB profiles in

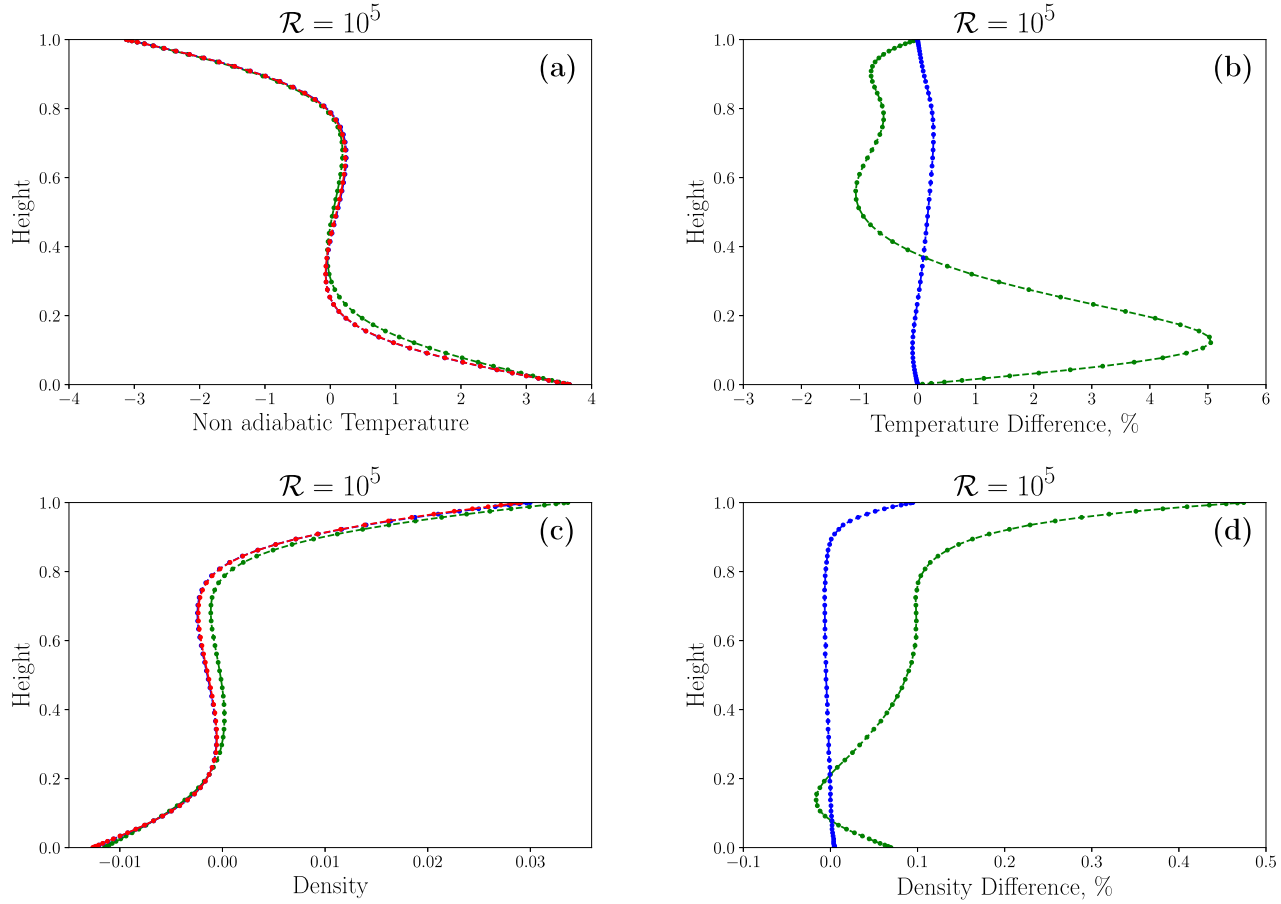

Figure 9. On the left-hand column mean temperature (top panel) and density (bottom panel) profiles minus the adiabatic contribution are depicted for the FC (red), AA (blue) and QB (green) cases for $\mathcal{R} = 10^5$. The different profiles being close together, we plot in the right-hand column (b and d) the differences between the approximated set of equations and the exact result [i.e. $(T_{\rm AA} - T_{\rm FC})/T_a$ in blue, $(T_{\rm QB} - T_{\rm FC})/T_a$ in green], in percentage of the adiabatic temperature or density (panels c and d) expected at the same depth.

blue and green, respectively. The right-hand column depicts the differences between the approximated profiles with the FC one in percentage of the adiabatic values [i.e. for the temperature, $(T_{\rm AA} - T_{\rm FC})/T_a$ in blue, $(T_{\rm QB} - T_{\rm FC})/T_a$ in green]. In each figure the top row represents temperature, the bottom one density.

At $\mathcal{R} = 10^5$, the differences between the different simulations are already small; at most 5 per cent differences in temperature and 0.5 per cent in density for the QB case, and basically five times smaller for the AA case. Increasing the $\mathcal{R}$ number ($\mathcal{R} = 10^8$ in Fig. 10) brings the AA simulation closer to the FC case. On the contrary the QB simulation does not come closer to the FC and appears colder and therefore much denser. In a strict Boussinesq case with a constant thermal expansivity, the average temperature would be centred. The behaviour of the QB case is easy to understand, following the arguments of Malkus (1954). Let us define ΔT_t, α_t and δ_t for the temperature jump, expansivity and thickness of the top boundary layer and ΔT_b, α_b and δ_b for the bottom boundary layer. The conservation of energy implies $\Delta T_t/\delta_t \approx \Delta T_b/\delta_b$ as the conductivity is uniform, while Malkus' hypothesis that the Rayleigh numbers of each boundary layer is critical requires $\Delta T_t \alpha_t \delta_t^3 \approx \Delta T_b \alpha_b \delta_b^3$. In the QB case, one therefore expects $\Delta T_b/\Delta T_t \approx (\alpha_t/\alpha_b)^{1/4}$ which is also $(\rho_t/\rho_b)^{(n-1)/4} = 1.35$ when the adiabatic values of densities are computed for our choice of dimensionless parameters. The corresponding increase in thickness of the bottom boundary layer shifts the bulk temperature to colder values. With $\Delta T_t + \Delta T_b = 6.79$ and $\Delta T_b/\Delta T_t = 1.35$, this shift with respect to the average temperature amounts to –0.51. As in addition, the choice of the adiabatic temperature shifts the FC temperature by 0.08, the bulk QB temperatures are colder than the FC predictions by ≈–0.6 in good agreement with Fig. 10(a). This temperature difference between QB and FC profiles does not change when $\mathcal{R} \geq 10^6$ but obviously, Malkus' hypothesis does not apply too close to the critical Rayleigh number (see Fig. 9a for $\mathcal{R} = 10^5$). The temperature jumps across the boundary layers and the average temperature cannot be correctly estimated with QB models.

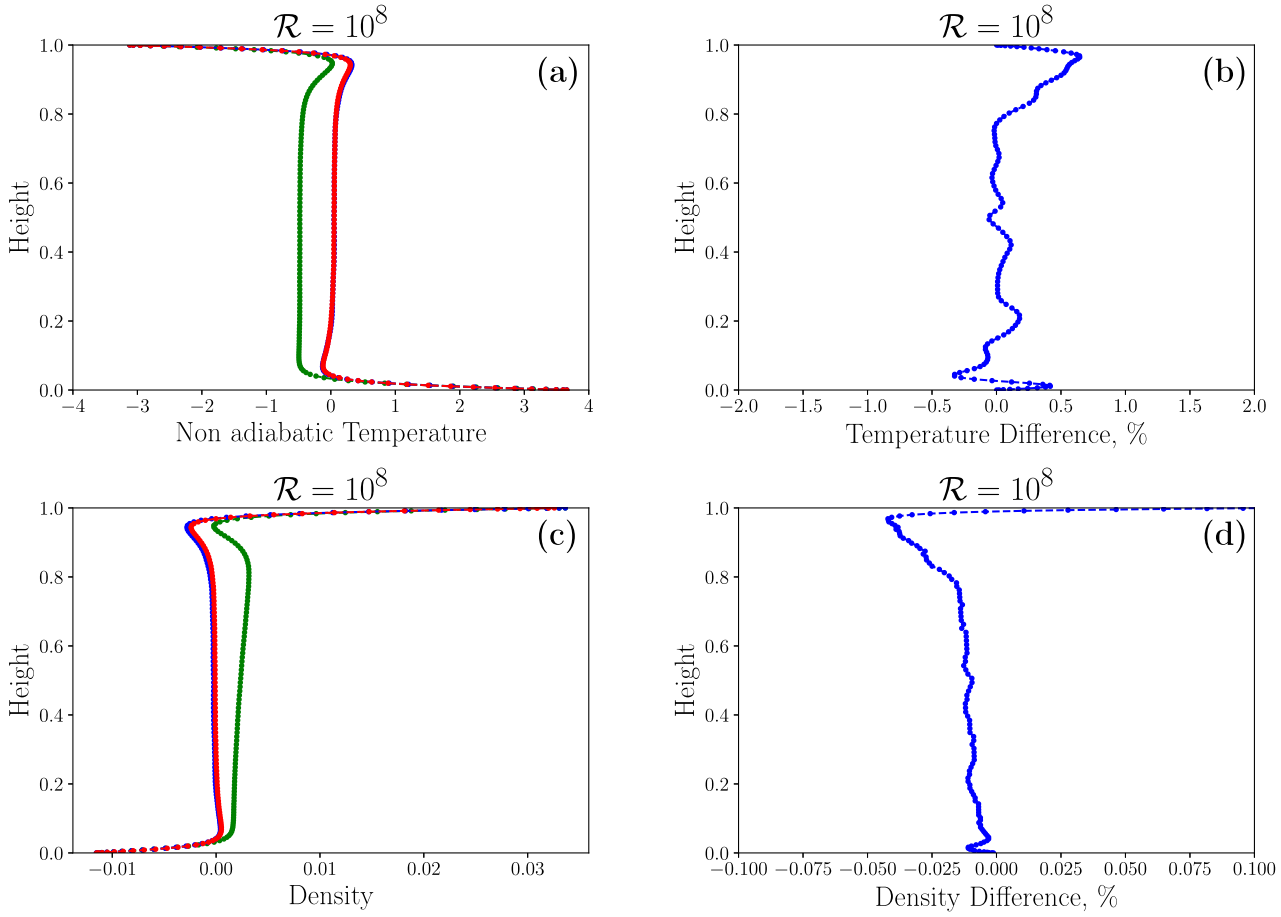

Figure 10. Same as Fig. 9 but for $\mathcal{R} = 10^8$. The decrease of thermal expansivity with depth thickens the bottom thermal boundary particularly in the QB case and also decreases the bulk temperature and increases the density (green). The FC (red) and AA (blue) cases are difficult to distinguish except maybe below the top boundary layer where the AA predicts slightly hotter and denser conditions. We do not plot the differences between QB and FC curves as their amplitudes are very large.

4.4 Heat transport

4.4.1 Analytical expressions

The transport of heat takes different forms depending on the equations that are used. In the FC case, the horizontal integration of $\mathbf{u}$ times the z-momentum (25b) implies, at all depth,

$$\overline{\mathbf{u}\cdot\boldsymbol{\nabla}\tau} - \overline{\mathbf{u}\cdot\boldsymbol{\nabla}P} = 0, \tag{46}$$

as FC mass conservation ensures $\overline{\rho w} = 0$. When the enthalpy $\mathcal{H}$ is introduced in the entropy eq. (25c) ($\mathrm{d}\mathcal{H} = T\mathrm{d}\mathcal{S} + \mathrm{d}P/\rho$), one gets (with dimensionless variables)

$$\frac{\mathrm{d}\overline{\rho w\mathcal{H}}}{\mathrm{d}z} - \frac{\mathcal{D}}{\mathcal{R}\epsilon}\overline{\mathbf{u}\cdot\boldsymbol{\nabla}P} = \frac{\mathcal{D}}{\mathcal{R}\epsilon}\overline{\tau:\boldsymbol{\nabla}\mathbf{u}} + \frac{\mathrm{d}^2\overline{T}}{\mathrm{d}z^2}, \tag{47}$$

and by combining these last two equations,

$$\frac{\mathrm{d}}{\mathrm{d}z}\left(\overline{\rho w\mathcal{H}} - \frac{\mathcal{D}}{\mathcal{R}\epsilon}\overline{u\tau_{xz} + w\tau_{zz}} - \frac{\overline{\mathrm{d}T}}{\mathrm{d}z}\right) = 0, \tag{48}$$

which expresses the conservation of a quantity that is obviously the total heat flux Q_{FC}

$$Q_{FC} = \overline{\rho w\mathcal{H}} - \frac{\mathcal{D}}{\mathcal{R}\epsilon}\overline{u\tau_{xz} + w\tau_{zz}} - \frac{\overline{\mathrm{d}T}}{\mathrm{d}z}. \tag{49}$$

The heat is therefore transported by the advection of enthalpy, by a work flow and a conductive term. The enthalpy term, $\overline{\rho w\mathcal{H}}$, involves $\overline{\rho C_V wT}$ present in the Boussinesq case (where $\rho C_V = \rho C_P$ is assumed to be constant) and additional contributions from temperature and density, namely $\alpha_0 K_T^0 \overline{wT}$ and $K_T^0(\overline{w\rho^n}/\rho_0^n)/(n-1)$, see eq. (13b). Besides, $C_V\overline{\rho wT}$ is also $C_V\overline{\rho wT'}$ as from the FC mass conservation

$C_V\overline{\rho w}T_a = 0$. When the flow becomes incompressible, $\mathcal{D} \to 0$, the density becomes function of temperature only (see eq. 17), the importance of the work flow vanishes and one also get $\overline{\rho w \mathcal{H}} \to \overline{\rho C_P w T}$ as it should (see eq. 21). The conductive term can also be split into two parts, the conductive transport of the non-adiabatic temperature $\overline{\mathrm{d}T'/\mathrm{d}z}$ which is only important in the top and bottom boundary layers and the conductive transport along the adiabat $\overline{\mathrm{d}T_a/\mathrm{d}z}$ present in the bulk of the fluid.

In the AA case, the equations are subtly different. In the momentum equation, the anelastic mass conservation only cancels the $\overline{\rho_a w} = \rho_a \overline{w}$ of the Stokes eq. (26b) but not the $\overline{\rho' w}$ term so that

$$\overline{\mathbf{u}\cdot\boldsymbol{\nabla}\tau} - \overline{\mathbf{u}\cdot\boldsymbol{\nabla}P} - \mathcal{R}\overline{\rho' w} = 0. \tag{50}$$

The enthalpy must then be expressed as a first order expansion of the exact expression (13b)

$$\mathcal{H} \approx \mathcal{H}_a + \mathcal{H}^{(1)}, \tag{51}$$

($\mathcal{H}^{(1)}$ is the first order expansion of $\mathcal{H}' = \mathcal{H} - \mathcal{H}_a$ in terms of ρ' and T', and therefore $\mathcal{H}^{(1)}$ and $\mathcal{H}'$ are identified in the AA case although they are slightly different in the FC case which contains higher order terms in temperature and density perturbations). $\mathcal{H}_a$ is obtained from (21) when the temperature and density are adiabatic. Its variation with depth is readily derived using (19a) and (19b), and leads to

$$\frac{\mathrm{d}\mathcal{H}_a}{\mathrm{d}z} = -\frac{\mathcal{D}}{\epsilon}, \tag{52}$$

while the first order expansion of the enthalpy (21) writes

$$\mathcal{H}^{(1)} = \left(1 + \frac{\Gamma_0}{\rho_a}\right) T' + \frac{\Gamma_0}{\epsilon\rho_a^2}\left(\rho_a^n - \epsilon T_a\right)\rho'. \tag{53}$$

The integration of the first order entropy equation then leads to

$$-\frac{\mathcal{D}}{\epsilon}\overline{\rho' w} + \frac{\mathrm{d}\overline{\rho w \mathcal{H}^{(1)}}}{\mathrm{d}z} - \frac{\mathcal{D}}{\mathcal{R}\epsilon}\overline{\mathbf{u}\cdot\boldsymbol{\nabla}P} = \frac{\mathcal{D}}{\mathcal{R}\epsilon}\overline{\tau : \boldsymbol{\nabla}\mathbf{u}} + \frac{\mathrm{d}^2\overline{T}}{\mathrm{d}z^2}, \tag{54}$$

which differs from the FC expression (47) as the transport of enthalpy is now divided in a transport along the adiabat and a transport due to fluctuations. The first term cancels with the extra $\overline{\rho' w}$ term of (50), and leads similarly to the FC case

$$Q_{AA} = \rho_a \overline{w\mathcal{H}^{(1)}} - \frac{\mathcal{D}}{\mathcal{R}\epsilon}\overline{u\tau_{xz} + w\tau_{zz}} - \overline{\frac{\mathrm{d}T}{\mathrm{d}z}}. \tag{55}$$

Again the first term is different from a simple advection of temperature $\rho_a C_V \overline{wT}$ (see eq. 53) and $\rho_a C_V \overline{wT} = \rho_a C_V \overline{wT'}$ as now the AA mass conservation implies $\rho_a C_V T_a \overline{w} = 0$. Our AA formalism leads, as it should, to a heat flow independent of depth. On the contrary, using the ALA formalism with constant heat capacities fails satisfying this condition as shown in Section 4.4.3.

Finally, in the QB case, the horizontal integration of the heat equation gives the well-known expression of the heat flow

$$Q_{QB} = \overline{wT} - \overline{\frac{\mathrm{d}T}{\mathrm{d}z}}, \tag{56}$$

that is the convective transport of temperature plus the conductive transport of temperature is constant through the convective layer. This is the classical Boussinesq balance which also holds for a variable expansivity (QB) that only appears in the Stokes equation, not in the energy balance.

4.4.2 Average heat transport

Fig. 11 depicts the various components of heat transport for the FC, AA and QB cases when $\mathcal{R} = 10^5$. In the QB case, the energy is only transported by temperature advection (mostly in the bulk of the fluid, in dashed–dotted red line) or by temperature conduction (mostly in the boundary layers, in blue). The sum of the two contributions is uniform with depth (green solid line) and carries a non-dimensional total heat flow $Q_{\mathrm{QB}} \approx 23$. Usually, the dimensionless heat flow, also known as the Nusselt number, Nu, is relative to the non-adiabatic temperature difference $\Delta T_{\mathrm{na}} = r - 1 - [T_a(1) - T_a(0)]$. Here the temperature being normalized by T_0 rather than ΔT_{na}, the heat flows that we compute are $\Delta T_{\mathrm{na}}/T_0 = 6.79$ larger than the Nusselt numbers. Adding the conduction along the adiabat to the convective and conductive Boussinesq heat fluxes (which is clearly non-physical) would increase the total heat flux to the green dotted line.

The situation is different for the FC and AA cases where various transport modes are possible. The enthalpy advection ($\overline{\rho w \mathcal{H}}$ for FC, or $\rho_a \overline{w\mathcal{H}^{(1)}}$ for AA in red dashed lines with large dots) is more intense in the bottom part of the fluid interior. This term differs, although moderately, from the heat flux transported by identifying the non-dimensional enthalpy and temperature ($\overline{\rho w T}$ or $\rho_a \overline{wT}$ are depicted with red dotted lines). The work-flow (green with dots) decreases the energy transport in the bottom half layer and increases it in the top half. Finally the adiabatic conduction (solid red) is also stronger near the surface where the adiabatic gradient is larger. The sum of the 4 contributors (enthalpy advection, work-flow, conduction along the non-adiabatic temperature and conduction along the adiabat) yields a uniform flow through depth (green solid line). The total heat flow of the FC and AA simulations are very similar ($Q_{\mathrm{FC}} \approx Q_{\mathrm{AA}} \approx 28$).

Fig. 12 is similar to Fig. 11 but $\mathcal{R}$ is now increased to $\mathcal{R} = 10^8$ (the cases $\mathcal{R} = 10^6$, $\mathcal{R} = 10^7$ and $\mathcal{R} = 10^9$ are shown as supplementary

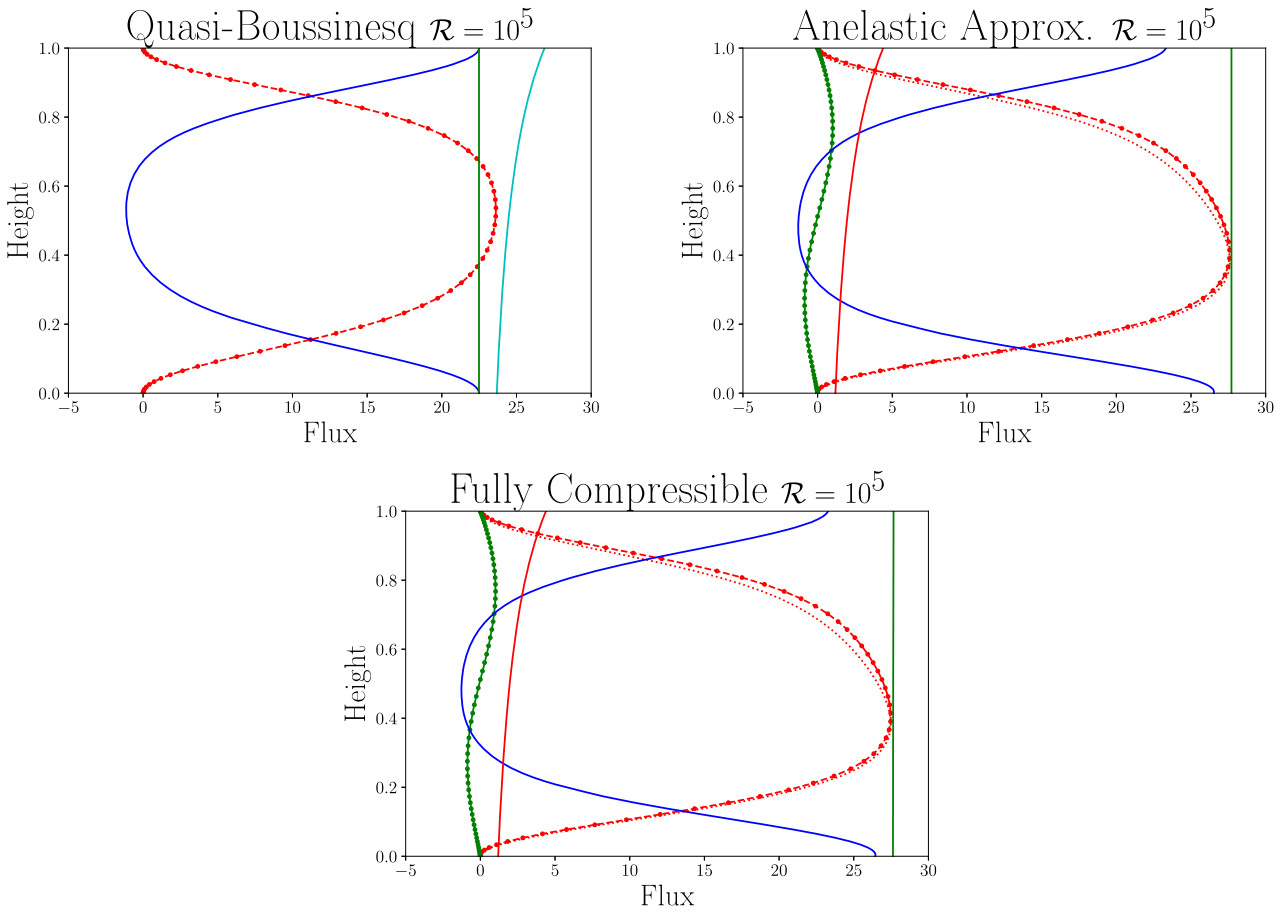

Figure 11. Different components of the heat flow profile across the convective layer. In the QB case the energy is transported by conduction (blue) or temperature advection (red dotted line). In the AA and FC case, we can distinguish the enthalpy advection (dashed–dotted red lines), the work flow (green dots), the conduction along the adiabat (solid red) and the conduction of the non-adiabatic temperature (solid blue). The sum of these components should be uniform with depth in statistical steady state (green line). We arbitrarily figure the adiabatic transport (cyan line) on top of the QB heat flow profile. The advection of temperature only is shown with thin dotted red lines in the AA and FC cases.

figures). Convection being much more chaotic and short wavelength than previously, it becomes difficult to compute accurately the statistically steady-state quantities and this explains the wiggles of the different profiles. The Nusselt number is around 185 for the FC and AA simulations, but like previously the heat flux is slightly lower for the QB case, around 175. The advection of enthalpy (red dashed lines with large dots for FC and AA, identified with the temperature in the QB case) is the main contributor to the heat flow transport in the three cases. In the FC and AA cases, this is particularly true in the deep layers. In the compressible FC and AA cases, the difference between enthalpy and temperature advection (dotted lines) is notable in the top half of the fluid. The work-flow (green with large dots) and the conduction along the adiabat (solid red) are minor components. Note that convection in the deep layers being more sluggish due to the reduced value of the thermal expansion coefficient, the conductive transport slightly increases with depth. This effect is balanced in the QB case by a convective transport of temperature increasing with height, while in the FC and AA cases, the convective transport of temperature only decreases with height (red dots) and an extra energy is transported by the total enthalpy (dashed–dotted red), work flow (green) and adiabatic conduction (red).

4.4.3 Heat flow assuming a constant C_P/C_V

To compare our AA equations with the ALA equations with constant C_P/C_V, we depict in Fig. 13 the total heat flow (see eq. 55) predicted when the systems of eqs (39c) (blue curves) or (40) (red curves) are used for the RHS of the energy equation. We recall that in the latter case, the entropy and temperature variations are assumed proportional with $\mathcal{S}' = C_P T'/T_a$ and C_P and C_V are identified and uniform. The different contributions to the heat flow (not shown) are roughly similar, but it is clear that the total heat flux is not uniform in the ALA approximation with constant heat capacities which confirms that the implemented equations are not consistent. The heat flow is invariably increasing with height in the bulk of the convective layer and lower in the two boundary layers. This inaccuracy is ultimately related to the fact that the expression of the entropy in $P-T$, $T-\rho$ and $\mathcal{H}-P$ variables are not consistent unless the proper behaviour of C_P/C_V is considered. In addition, the ALA heat flow with constant C_P is larger by ≈4 per cent, compared to the AA case.

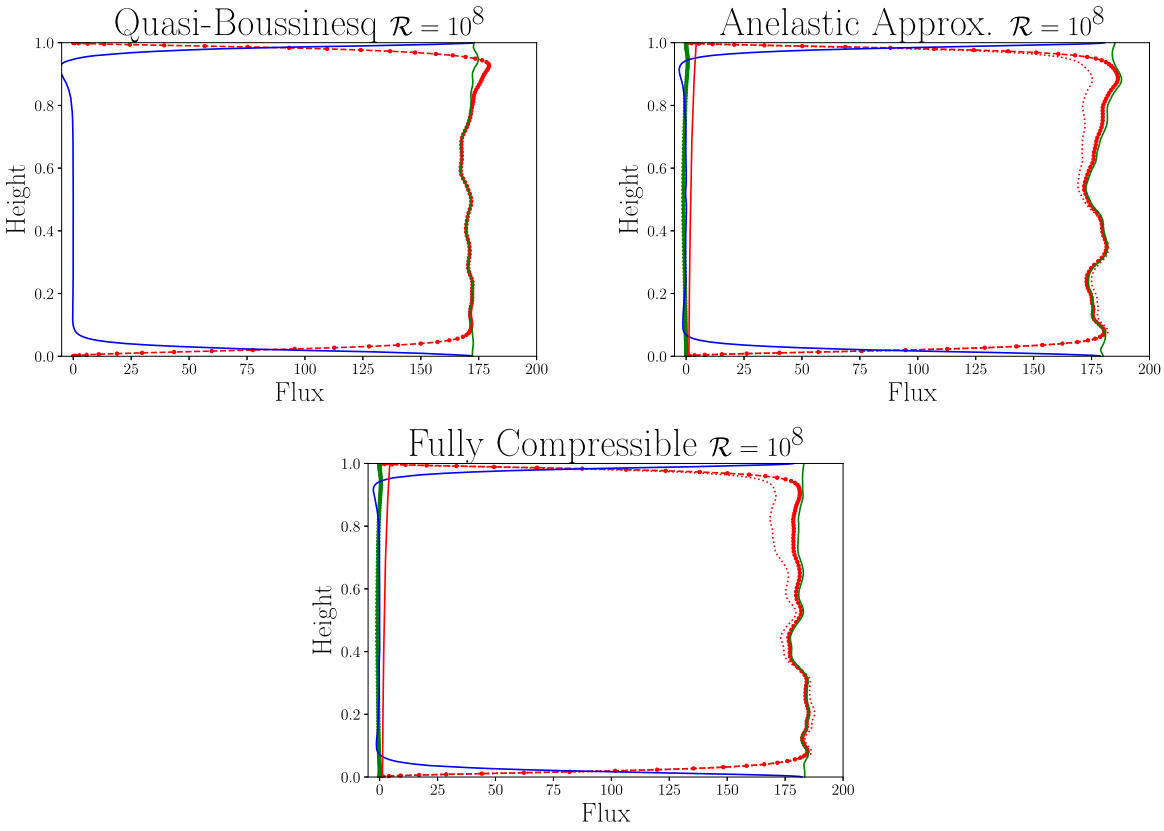

Figure 12. Similar to Fig. 11 but for $\mathcal{R} = 10^8$. The convection is short wavelength and very vigorous and it becomes more difficult to get accurate statistical values. The total heat flow (green lines) is reasonably uniform.

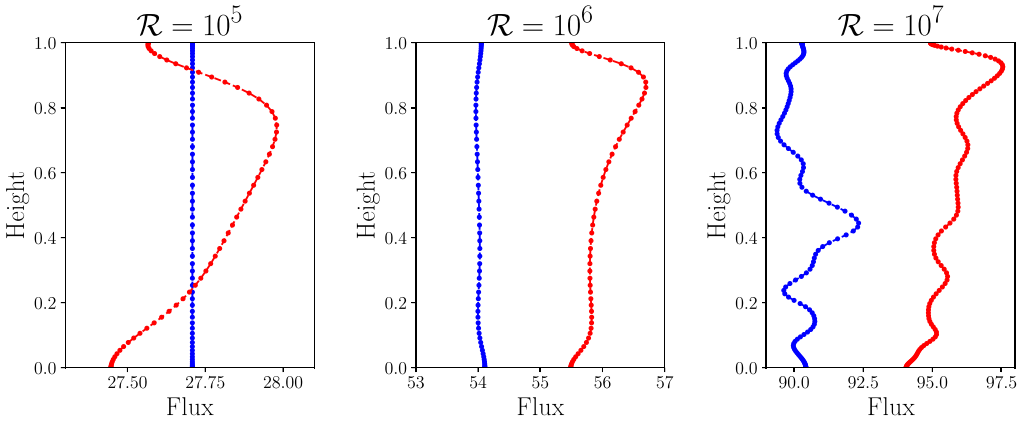

Figure 13. Heat flow profiles. Note the small range of the horizontal scales. The classical anelastic eqs (40) where the entropy is only related to temperature (ALA) and where the heat capacity ratio C_P/C_V is approximated as uniform leads to the heat flow depicted with red lines. Our formalism when the heat equation is (39c), leads to the predictions in blue. The inconsistency in the thermodynamics leads to a non-uniform heat flux increasing with height in the convective region and a surface heat flow overestimated by ≈4 per cent at large $\mathcal{R}$ number.

4.5 Dissipation

4.5.1 Total dissipation

Another interesting quantity within the convection volume is the dissipation. Following Hewitt *et al.* (1975) we define dissipation as

$$\mathcal{D}iss = \frac{\mathcal{D}}{\mathcal{R}\epsilon}\dot{\varepsilon} : \tau, \tag{57}$$

which according to (26c) can be directly compared to the diffusive term of the entropy equation. Dissipation appears locally as an effective heat source non-uniformly distributed (Trubitsyn & Trubitsyn 2020). Dissipation also plays an important role in localizing the deformation

in the lithosphere (Fleitout & Froidevaux 1980) and potentially in controlling the overall rheology of the mantle by limiting the mantle grain size (Ricard & Bercovici 2009). Dissipation is also a measure of the energy transported in a convective fluid and this has been used to put bounds on core dynamos (Buffett 2002; Labrosse 2003), although in this case ohmic dissipation dominates viscous dissipation.

The total dissipation in a convective fluid can be expressed by integration of the Stokes or entropy FC equations as

$$\langle \mathcal{D}iss \rangle = -\frac{\mathcal{D}}{\mathcal{R}\epsilon}\left\langle \frac{\mathrm{D}P}{\mathrm{D}t}\right\rangle = \left\langle \rho T \frac{\mathrm{D}\mathcal{S}}{\mathrm{D}t}\right\rangle = -\left\langle \rho \mathcal{S}\frac{\mathrm{D}T}{\mathrm{D}t}\right\rangle, \tag{58}$$

where $\langle . \rangle$ is the statistically steady state quantities, averaged in time and integrated over the volume (Verhoogen 1981; Alboussière & Ricard 2013). In the last equality, $\rho \mathcal{S}\mathrm{D}T/\mathrm{D}t$ should be close to $\rho_a w \mathcal{S}(\mathrm{d}T_a/\mathrm{d}z)$ as $\mathcal{S}$ is close to zero and ρ and T close to the adiabatic reference at high Rayleigh numbers. One therefore expects that

$$\langle \mathcal{D}iss \rangle \approx \mathcal{D}\left\langle \frac{T_a w \mathcal{S}}{\rho_a^{n-1}\gamma_a}\right\rangle. \tag{59}$$

In the QB case, the integration of $\mathbf{u}$ times the Stokes eq. (41b) leads to a simple exact equation

$$\langle \mathcal{D}iss \rangle = \mathcal{D}\left\langle \frac{wT}{\rho_a^{n-1}}\right\rangle. \tag{60}$$

In the classical Boussinesq case where thermal expansivity is uniform, the ρ_a term is absent from (60) and $\langle wT \rangle$ is just the convective heat flow $Q_{\mathrm{BA}} - \Delta T$ according to (56), or, if we neglect the conductive contribution at high Rayleigh number $\langle wT \rangle \approx Q_{\mathrm{BA}}$. We therefore expect

$$\frac{\langle \mathcal{D}iss \rangle}{\mathcal{D}Q_{BA}} \approx 1. \tag{61}$$

In the absence of an exact expression relating dissipation and heat flow for the FC case, we may guess that $\langle \mathcal{D}iss \rangle/(\mathcal{D}Q_{FC})$ still remains of order 1 and presumably lower due to the presence of $1/\rho_a^{n-1} \leq 1$ in the averaging (see (60)).

No analytical results are available for the profile of dissipation with depth, $\overline{\mathcal{D}iss}$, however the eqs (59) suggests a fundamental relation with the entropy transport in compressible convection that we will now emphasize. In a companion paper (Alboussière *et al.* 2022) and with very specific and different EoS, the role of entropy transport is also discussed.

4.5.2 A conjecture for the dissipation profile?

The equations that express the heat flow transport (46) and (47) can be reformulated in a way that we have not seen in the literature. Introducing the Gibbs free energy $\mathcal{G} = \mathcal{H} - T\mathcal{S}$, the total heat flow (49) is also

$$Q_{FC} = \overline{\rho w T \mathcal{S}} + \left(\overline{\rho w \mathcal{G}} - \frac{\mathcal{D}}{\mathcal{R}\epsilon}\overline{u\tau_{xz} + w\tau_{zz}}\right) - \overline{\frac{\partial T}{\partial z}}. \tag{62}$$

From basic rules of thermodynamics one has

$$\rho \frac{\mathrm{D}\mathcal{G}}{\mathrm{D}t} = -\rho \mathcal{S}\frac{\mathrm{D}T}{\mathrm{D}t} + \frac{\mathrm{D}P}{\mathrm{D}t}, \tag{63}$$

that leads after horizontal integration using mass conservation (and using dimensionless variables)

$$\frac{\mathrm{d}\overline{\rho w \mathcal{G}}}{\mathrm{d}z} = -\overline{\rho \mathcal{S}\frac{\mathrm{D}T}{\mathrm{D}t}} + \frac{\mathcal{D}}{\mathcal{R}\epsilon}\overline{\mathbf{u}\cdot\boldsymbol{\nabla}P}. \tag{64}$$

The expression of $\overline{\mathbf{u}\cdot\boldsymbol{\nabla}P}$ derived from this equation can be introduced into (46), and yields

$$\overline{\mathcal{D}iss} = \overline{\rho \mathcal{S}\frac{\mathrm{D}T}{\mathrm{D}t}} - \frac{\mathrm{d}}{\mathrm{d}z}\left(\overline{\rho w \mathcal{G}} - \frac{\mathcal{D}}{\mathcal{R}\epsilon}\overline{u\tau_{xz} + w\tau_{zz}}\right), \tag{65}$$

and finally, using the expression for the adiabatic gradient,

$$\overline{\mathcal{D}iss} = \mathcal{D}\overline{\frac{wT\mathcal{S}}{\rho^{n-1}\gamma_a}} + \overline{\rho \mathcal{S}\left(\frac{\mathrm{D}T}{\mathrm{D}t} - \frac{\mathcal{D}wT}{\rho^n \gamma_a}\right)} - \frac{\mathrm{d}}{\mathrm{d}z}\left(\overline{\rho w \mathcal{G}} - \frac{\mathcal{D}}{\mathcal{R}\epsilon}\overline{u\tau_{xz} + w\tau_{zz}}\right). \tag{66}$$

We can now compare the equations for the heat flow (62) and the viscous dissipation (66) and discuss the order of magnitude of the different terms. The conduction (last term of eq. 62) is certainly very small in the bulk, at large values of the Rayleigh number. The second term on the RHS of eq. (66) is also likely small as $\mathcal{S}$ is small and multiplied by a term which cancels in adiabatic conditions. Then, both expressions include the Gibbs free energy and a work flow that is found very small in our simulations. We propose that at large enough Rayleigh numbers, the Gibbs energy and work flow contribution are both negligible compared to the entropy transport and that in FC convection, the heat flux and dissipation profiles become

$$Q_{FC} \approx \overline{\rho w T \mathcal{S}} \approx \rho_a T_a \overline{w \mathcal{S}}, \tag{67}$$

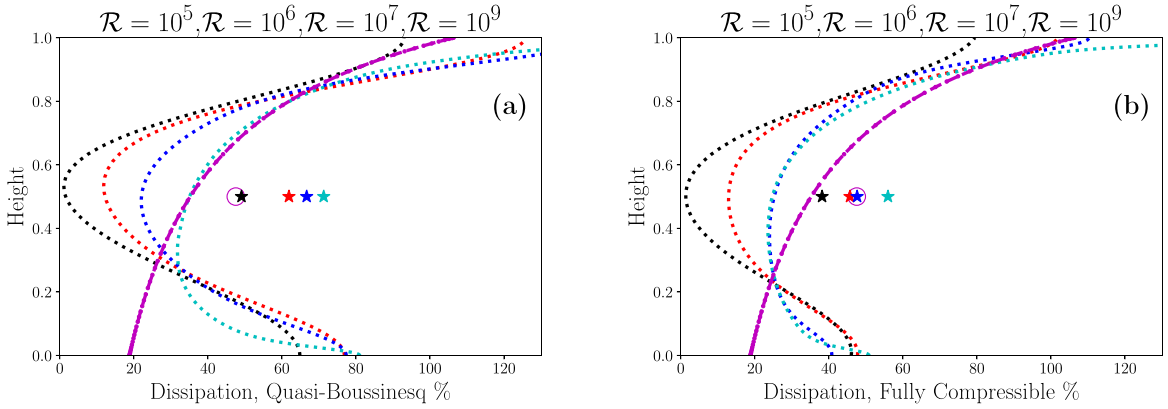

Figure 14. Normalized dissipations in percent, computed for the QB (a) and FC (b) formalisms, at different $\mathcal{R}$ numbers. The stars show the average normalized dissipations which as expected from eq. (61) are smaller than 100 per cent. The black, red, blue, cyan curves are for $\mathcal{R} = 10^5$, 10^6, 10^7, 10^9, respectively. The dashed magenta curve is $1/(\rho_a^n \gamma_a)$ that might be the limiting case of the dissipation profile in the bulk of the fluid, at very large $\mathcal{R}$. Its average is shown by a magenta circle.

$$\overline{\mathcal{D}iss} \approx \mathcal{D} \frac{\overline{wT\mathcal{S}}}{\rho^{n-1}\gamma_a} \approx \frac{\mathcal{D}}{\rho_a^{n-1}\gamma_a} T_a \overline{w\mathcal{S}}, \tag{68}$$

where we replaced ρ and T by their adiabatic values as $\mathcal{S}$ is close to zero. We therefore suggest that

$$\overline{\mathcal{D}iss} \approx \frac{\mathcal{D}}{\rho_a^n \gamma_a} Q_{FC}, \tag{69}$$

meaning that at each depth, the average flux of entropy is dissipated. If this balance, that should hold at large Rayleigh number is true, then, not only the total dissipation can be related to the surface heat flow (eq. 59), but at each horizontal depth the average dissipation can be related to the total flux times a function of the adiabatic properties. This depth dependent equilibrium is also in agreement with the volume integrated condition (eq. 59). The balance expressed by eq. (69) assumes that g is constant, but similar results should be expected when g is depth-dependent, and a normalized depth dependent gravity should multiply the right-hand side of eq. (69).

Fig. 14 depicts the profiles of the normalized dissipations $\overline{\mathcal{D}iss}/\mathcal{D}Q$ in per cent, for the QB and FC cases (the AA cases being quite similar to the FC cases) computed for $\mathcal{R}$ numbers of 10^5, 10^6, 10^7 and 10^9. The volume averaged dissipations are shown with the stars and they are smaller than 1 as expected from eq. (59). We suggest that the magenta curve [i.e. $g/(\rho_a^n \gamma_a)$ in per cent] might be the limit of the dissipation profile of FC convection at high Rayleigh number (panel b). This guess obviously is not valid in the non-convective boundary layers. If this guess is true, the convergence toward this limit is at any rate, very slow. This asymptotic estimate does not hold for the QB case (panel a) where the dissipation is larger and seems above the magenta line at high $\mathcal{R}$ numbers.

5 DISCUSSION AND CONCLUSION

In the infinite Prandtl number convection case (convection without inertia) where the sound waves cannot propagate, it does not appear much more difficult to compute a simulation with the FC equations than using the AA. A choice of an appropriate EoS allows all the terms needed by the formalism to be computed and the Murnaghan EoS with a Grüneisen parameter varying as the inverse of density seems a flexible and accurate choice. Although we are certainly not the first ones to start with a Murnaghan EoS (e.g. Glatzmaier 1988; Bercovici *et al.* 1989, 1992; Bunge *et al.* 1997), all previous authors seem to have added additional approximations (such as constant parameters) that were not necessary. Various ingredients of planetary dynamics are not considered in our 2-D simulations, such as 3-D geometry, sphericity, depth dependence of gravity, viscosity or conductivity but should be easily implemented (although the computation time would largely increase). Phase transitions are also an important ingredient of mantle convection. If they can be considered as pure univariant discontinuities they might be included by matching solutions across the phase transition (e.g. like in Christensen & Yuen 1984; Chambat *et al.* 2014).

The FC formalism avoids a number of difficulties, the major one being the difficulty to assess properly the quality of the approximations that are done by implementing the anelastic formalism. In addition to the inconsistencies that were previously pointed to (e.g. by Leng & Zhong 2008), we met two other problems with the AA. First, we had to impose the conservation of the total mass to avoid a drift of this quantity during the simulations (see eq. 45). We suppose that mass conservation was also enforced in previous simulations although we have not seen this subject discussed in the geophysical literature. A second problem was related to the appearance of both C_V and C_P in the equations. Although C_P and C_V have similar values, their ratio cannot be constant and its variation with pressure and temperature should be taken into account, something already noted by Alboussière & Ricard (2013). When the two heat capacities are confused, a correct interpretation of the transported heat flow becomes impossible and the heat flow is unphysically varying with depth (see Fig. 13).

Another problem that we encountered and appears both in the FC and AA cases, is with the choice of the adiabatic gradient. This choice constrains the total mass included in the convective layer and as the simulations are done with fixed boundaries, one cannot be sure before a statistically steady state surface pressure is computed, that the average pressure at the surface, or the average density, are close to the values required by the boundary conditions. This problem is solved in our models by adjusting the reference temperature in a few iterations.

The QB case is, not surprisingly, rather far away from the FC calculations. The relative thicknesses of the boundary layers are inaccurate and adding, *a posteriori*, an adiabatic profile to the non-compressible simulation is incoherent. Furthermore there is no indication on how to choose an appropriate surface adiabatic temperature. The AA and FC simulations lead to very similar results. Note however that our AA equations are not those of the usual ALA formalism that we found inaccurate when the two heat capacities are identified. The similarity of the AA and FC simulations comes from the fact that in the bulk of the convective fluid, the departures from adiabaticity are indeed small and in the boundary layers where these departures are very large, the behaviour is simply controlled by diffusion and compressible effects are negligible. AAs are also commonly made with convection heated from within by radiogenic sources (e.g. Schubert *et al.* 2001). In this case however, the final temperatures are known to be significantly colder and far from adiabaticity at depth (Bunge *et al.* 2001). One could guess that in mantle convection where the importance of internal sources (or of secular cooling) is large, the differences between FC and AA solutions might be larger.

During the comparisons of the heat flows profiles, we propound that the dissipation profile may be derived directly from the total heat flow and the adiabatic profile, as both dissipation and heat flow are related to the transport of entropy at high enough Rayleigh number. We cannot prove this result analytically, however our FC and AA simulations suggest that this equilibrium provides a useful proxy of the dissipation profile. This behaviour does not seem to be verified by the QB simulations.

The AA remains necessary for the situations where inertia is non-negligible in the momentum equation, that is where sound waves must be filtered out, such as in the fluid core of the Earth. FC convection with a finite Prandlt number is not considered in this paper. Fortunately the AA and FC simulations give very similar values particularly with the high Rayleigh numbers of planetary fluid layers. We suggest however that the Murnaghan EoS remains a rather accurate EoS that should be used to properly express all the thermodynamic terms needed in the equations. The shape of the adiabatic profiles derived from this EoS are very different from the exponential profiles, that are often used and derived from (6a) when all the reference adiabatic values are assumed constant (see e.g. King *et al.* 2010). Working with realistic EoS and thermodynamic quantities is highly necessary when the results are applied to extrasolar planets where the compressibility effects may be much larger than on Earth. We however specifically show that with the Murnaghan EoS, the effective dissipation number should never attain very large values (see eq. 24).

ACKNOWLEDGMENTS

The authors are grateful to the LABEX Lyon Institute of Origins (ANR-10-LABX-0066) of the Université de Lyon for its financial support within the program ANR-11-IDEX-0007 of the French government operated by the French National Research Agency (ANR). Support was provided by the ICMAT Severo Ochoa Project No. SEV-2015-0554. JC also acknowledges the support of the RyC project RYC2018-025169, the Spanish grant [PID2020-114043GB-I00] and the Catalan Grant [No. 2017SGR1049]. We thank Pr Masanori Kameyama and the other reviewer for their thorough and constructive comments.

DATA AVAILABILITY

No new data were generated or analysed in support of this research. The numerical codes using the Dedalus software are available on demand or at the address https://github.com/RayleighBenardModels/Compressible_Murnaghan.

REFERENCES

Alboussière, T., Curbelo, J., Dubuffet, F., Labrosse, S. & Ricard, Y., 2022. Compressible convection playground: a playground for compressible natural convection with a nearly uniform density, *J. Fluid Mech.,* in press.

Alboussière, T. & Ricard, Y., 2013. Reflections on dissipation associated with thermal convection, *J. Fluid Mech.,* **751**(R1), 749–751.

Alfe, D., Price, G. & Gillan, M., 2002. Iron under Earth's core conditions: liquid-state thermodynamics and high-pressure melting curve from ab initio calculations, *Phys. Rev. B,* **65**(16).

Anderson, O., Oda, H. & Isaak, D., 1992. A model for the computation of thermal expansivity at high compression and high-temperatures—MgO as an example, *Geophys. Res. Lett.,* **19**(19), 1987–1990.

Anderson, O.L., 1979. Evidence supporting the approximation $\gamma\rho = \text{const}$ for the Grüneisen parameter of the Earth lower mantle, *J. geophys. Res.,* **84,** 3537–3542.

Anderson, O.L., 2000. The Grüneisen ratio for the last 30 years, *Geophys. J. Int.,* **143,** 279–294.

Anufriev, A., Jones, C. & Soward, A., 2005. The Boussinesq and anelastic liquid approximations for convection in the Earth's core, *Phys. Earth planet. Inter.,* **152**(3), 163–190.

Anzellini, S., Dewaele, A., Mezouar, M., Loubeyre, P. & Morard, G., 2013. Melting of iron at Earth's inner core boundary based on fast X-ray diffraction, *Science,* **340**(6131), 464–466.

Ascher, U., Ruuth, S. & Spiteri, R., 1997. Implicit-explicit Runge-Kutta methods for time-dependent partial differential equations, *App. Num. Math.,* **25**(2–3), 151–167.

Bercovici, D., Schubert, G. & Glatzmaier, G.A., 1989. 3-dimensional spherical-models of convection in the Earths mantle, *Science,* **244,** 950–955.

Bercovici, D., Schubert, G. & Glatzmaier, G.A., 1992. 3-dimensional convection of an infinite-Prandtl-number compressible fluid in a basally heated spherical-shell, *J. Fluid Mech.,* **239,** 683–719.

Blankenbach, B. *et al.*, 1989. A benchmark comparison for mantle convection codes, *Geophys. J. Int.,* **98**(1), 23–38.

Boehler, R., 1993. Temperatures in the Earth's core from melting-point measurements of iron at high static pressures, *Nature,* **363**(6429), 534–536.
Boussinesq, J., 1903. *Théorie analytique de la chaleur, tome 2,* Gauthier-Villars.
Braginsky, S. & Roberts, P., 1995. Equations governing convection in Earth's core and the geodynamo, *Geophys. Astrophys. Fluid Dyn.,* **79**(1–4), 1–97.
Brown, J. & Shankland, T., 1981. Thermodynamic parameters in the Earth as determined from seismic profiles, *Geophys. J. R. astr. Soc.,* **66**(3), 579–596.
Buffett, B., 2002. Estimates of heat flow in the deep mantle based on the power requirements for the geodynamo, *Geophys. Res. Lett.,,* **29**(12), 7–1-7-4.
Bunge, H.P., Ricard, Y. & Matas, J., 2001. Non-adiabaticity in mantle convection, *Geophys. Res. Lett.,,* **28,** 879–882.
Bunge, H.P., Richards, M.A. & Baumgardner, J.R., 1997. A sensitivity study of three-dimensional spherical mantle convection at 10^8 Rayleigh number: Effects of depth-dependent viscosity, heating mode, and an endothermic phase change, *J. geophys. Res.,* **102,** 11 991–12 007.
Burns, K.J., Vasil, G.M., Oishi, J.S., Lecoanet, D. & Brown, B.P., 2020. Dedalus: a flexible framework for numerical simulations with spectral methods, *Phys. Rev. Res.,* **2,**.
Busse, F. *et al.*, 1994. 3d convection at infinite Prandtl number in Cartesian geometry—a benchmark comparison, *Geophys. Astrophys. Fluid Dyn.,* **75**(1), 39–59.
Chambat, F., Benzoni-Gavage, S. & Ricard, Y., 2014. Jump conditions and dynamic surface tension at permeable interfaces such as the inner core boundary, *C. R. Geosci.,* **346**(5–6), 110–118.
Choblet, G., Cadek, O., Couturier, F. & Dumoulin, C., 2007. OEDIPUS: a new tool to study the dynamics of planetary interiors, *Geophys. J. Int.,* **170**(1), 9–30.
Chopelas, A. & Boehler, R., 1992. thermal expansivity in the lower mantle, *Geophys. Res. Lett.,* **19**(19), 1983–1986.
Christensen, U.R. & Yuen, D.A.., 1984. the interaction of a subducting lithospheric slab with a chemical or phase-boundary, *J. geophys. Res.,* **89,** 4389–4402.
Curbelo, J., Duarte, L., Alboussière, T., Dubuffet, F., Labrosse, S. & Ricard, Y., 2019. Numerical solutions of compressible convection with an infinite Prandtl number: comparison of the anelastic and anelastic liquid models with the exact equations, *J. Fluid Mech.,* **873,** 646–687.
Currie, L.K. & Browning, M.K., 2017. The magnitude of viscous dissipation in strongly stratified two-dimensional convection, *Astrophys. J. Lett.,* **845**(2), doi:10.3847/2041-8213/aa8301.
Dubuffet, F., Yuen, D.A. & Rabinowicz, M., 1999. Effects of a realistic mantle thermal conductivity on the patterns of 3-D convection, *Earth planet. Sci. Lett.,* **171,** 401–409.
Duffy, T. & Ahrens, T., 1993. Thermal-expansion of mantle and core materials at very high-pressures, *Geophys. Res. Lett.,* **20**(11), 1103–1106.
Fleitout, L. & Froidevaux, C., 1980. Thermal and mechanical evolution of shear zones, *J. Struct. Geol.,* **2**(1–2), 159–164.
Funamori, N., Yagi, T., Utsumi, W., Kondo, T., Uchida, T. & Funamori, M., 1996. Thermoelastic properties of $MgSiO_3$ perovskite determined by in situ X ray observations up to 30 GPa and 2000 K, *J. geophys. Res.,* **101**(B4), 8257–8269.
Gassmoller, R., Dannberg, J., Bangerth, W., Heister, T. & Myhill, R., 2020. On formulations of compressible mantle convection, *Geophys. J. Int.,* **221**(2), 1264–1280.
Glatzmaier, G.A., 1988. Numerical simulation of mantle convection: time-dependent, three dimensional, compressible,spherical shell, *Geophys. Astrophys. Fluid Dyn.,* **43,** 223–264.
Gubbins, D., Alfè, D., Masters, G., Price, G.D. & Gillan, M.J., 2003. Can the Earth's dynamo run on heat alone?, *Geophys. J. Int.,* **155**(2), 609–622.
Hansen, U., Yuen, D.A., Kroening, S.E. & Larsen, T.B., 1993. Dynamic consequences of depth-dependent thermal expansivity and viscosity on mantle circulations and thermal structure, *Phys. Earth planet. Inter.,* **77,** 205–223.
Hewitt, J.M., McKenzie, D.P. & Weiss, N.O., 1975. Dissipative heating in convective flows, *J. Fluid Mech.,* **68,** 721–738.
Jarvis, G.T. & McKenzie, D.P., 1980. Convection in a compressible fluid with infinite Prandtl number, *J. Fluid Mech.,* **96,** 515–583.
Kameyama, M. & Yamamoto, M., 2018. Numerical experiments on thermal convection of highly compressible fluids with variable viscosity and thermal conductivity: implications for mantle convection of super-Earths, *Phys. Earth planet. Inter.,* **274,** 23–36.
Katsura, T., Yoneda, A., Yamazaki, D., Yoshino, T. & Ito, E., 2010. Adiabatic temperature profile in the mantle, *Phys. Earth planet. Inter.,* **183**(1–2, SI), 212–218.
King, S.D., Lee, C., van Keken, P.E., Leng, W., Zhong, S., Tan, E., Tosi, N. & Kameyama, M.C., 2010. A community benchmark for 2-D Cartesian compressible convection in the Earth's mantle, *Geophys. J. Int.,* **180**(1), 73–87.
Labrosse, S., 2003. Thermal and magnetic evolution of the Earth's core, *Phys. Earth Planet. Inter.,* **140**(1–3), 127–143.
Lantz, S. & Fan, Y., 1999. Anelastic magnetohydrodynamic equations for modeling solar and stellar convection zones, *Astrophys. J.,* **121**(1), 247–264.
Lecoanet, D., Brown, B.P., Zweibel, E.G., Burns, K.J., Oishi, J.S. & Vasil, G.M., 2014. Conduction in low Mach number flows. I. Linear and weakly nonlinear regimes, *Astrophys. J.,* **797**(2),.
Leng, W. & Zhong, S., 2008. Viscous heating, adiabatic heating and energetic consistency in compressible mantle convection, *Geophys. J. Int.,* **173**(2), 693–702.
Machetel, P. & Yuen, D.A., 1989. Penetrative convective flows induced by internal heating and mantle compressibility, *J. geophys. Res.,* **94,** 10 609–10 626.
Malkus, W., 1954. The heat transport and spectrum of thermal turbulence, *Proc. Royal Soc. Lond., A,* **225**(1161), 196–212.
Murnaghan, F.D., 1951. *Finite Deformation of an Elastic Solid,* John Wiley and Sons.
Oberbeck, A., 1879. Über die wärmeleitung des flüssigkeiten bei berücksichtigung des strömungen infolge von temperaturdifferenzen, *Ann. Phys. Chem.,* **7,** 271–292.
Ogura, Y. & Phillips, N., 1962. Scale analysis of deep and shallow convection in the atmosphere, *J. Atmos. Sci.,* **19**(2), 173–179.
Parmentier, E. & Sotin, C., 2000. Three-dimensional numerical experiments on thermal convection in a very viscous fluid: implications for the dynamics of a thermal boundary layer at high Rayleigh number, *Phys. Fluids,* **12**(3), 609–617.
Petit, A.T. & Dulong, P.L., 1819. Recherches sur quelques points importants de la théorie de la chaleur, *Annal. Chim. Phys.,* **10,** 395–413.
Ricard, Y., 2015. 7.02 - Physics of mantle convection, *Treatise on Geophysics,* 2nd edn, pp. 31–87, ed.Schubert, G., Elsevier.
Ricard, Y. & Bercovici, D., 2009. A continuum theory of grain size evolution and damage, *J. geophys. Res.,* **114**(B1), doi:10.1029/2007JB005491.
Ricard, Y., Labrosse, S. & Dubuffet, F., 2014. Lifting the cover of the cauldron: convection in hot planets, *Geochem. Geophys. Geosyst.,* **15**(12), 4617–4630.
Rolf, T., Coltice, N. & Tackley, P.J., 2012. Linking continental drift, plate tectonics and the thermal state of the Earth's mantle, *Earth planet. Sci. Lett.,* **351,** 134–146.
Schmeling, H., Marquart, G. & Ruedas, T., 2003. Pressure- and temperature-dependent thermal expansivity and the effect on mantle convection and surface observables, *Geophys. J. Int.,* **154,** 224–229.
Schubert, G., Turcotte, D. & Olson, P., 2001. *Mantle Convection in the Earth and Planets,* Cambridge Univ. Press.
Solheim, L. & Peltier, W., 1990. Heat-transfer and the onset of chaos in a spherical, axisymmetrical, anelastic model of whole mantle convection, *Geophys. Astrophys. Fluid Dyn.,* **53**(4), 205–255.
Stacey, F.D., 1977. Application of thermodynamics to fundamental earth physics, *Geophys. Surv.,* **3,** 175–204.
Stacey, F.D. & Davis, P.M., 2004. High pressure equations of state with applications to the lower mantle and core, *Phys. Earth planet. Inter.,* **142,** 137–184.
Stixrude, L. & Lithgow-Bertelloni, C., 2005. Thermodynamics of mantle minerals - I. Physical properties, *Geophys. J. Int.,* **162**(2), 610–632.

Tackley, P.J., 2008. Modelling compressible mantle convection with large viscosity contrasts in a three-dimensional spherical shell using the yin-yang grid, *Phys. Earth planet. Inter.,* **171**(1–4, SI), 7–18.

Tan, E. & Gurnis, M., 2007. Compressible thermochemical convection and application to lower mantle structures, *J. geophys. Res.,* **112**(B6), doi:10.1029/2006JB004505.

Trubitsyn, A.P. & Trubitsyn, V.P., 2020. Compressibility, dissipation, and heat sources effect on temperature and heat flow distribution in the Earth's Mantle, *Izvestiya-Phys. Solid Earth,* **56**(6), 729–736.

Trubitsyn, V.P. & Trubitsyn, A.P., 2015. Effects of compressibility in the mantle convection equations, *Izvestiya-Phys. Solid Earth,* **51**(6), 801–813.

Verhoeven, J., Wiesehoefer, T. & Stellmach, S., 2015. Anelastic versus fully compressible turbulent Rayleigh-Benard convection, *Astrophys. J.,* **805**(1),.

Verhoogen, J., 1981. *Energetics of the Earth,* National Academy of Sciences.

Wolf, A.S., Jackson, J.M., Dera, P. & Prakapenka, V.B., 2015. The thermal equation of state of (Mg, Fe)SiO_3 bridgmanite (perovskite) and implications for lower mantle structures, *J. geophys. Res.,* **120**(11), 7460–7489.

Yoshida, M., 2017. On approximations of the basic equations of terrestrial mantle convection used in published literature, *Phys. Earth planet. Inter.,* **268,** 11–17.

Zhong, S., McNamara, A., Tan, E., Moresi, L. & Gurnis, M., 2008. A benchmark study on mantle convection in a 3-D spherical shell using CitcomS, *Geochem. Geophys. Geosys.,* **9,** doi:10.1029/2008GC002048.

SUPPORTING INFORMATION

Supplementary data are available at *GJI* online.

Figure S1. Quasi-Boussinesq and anelastic approximations. Mean temperature (left-hand column) and density (right-hand column) profiles for $\mathcal{R} = 10^5$.

Figure S2. Quasi-Boussinesq and anelastic approximations, fully compressible case. Mean temperature (left-hand column) and density (right-hand column) profiles for $\mathcal{R} = 10^6$.

Figure S3. Different components of the heat flow profile across the convective layer for $\mathcal{R} = 10^6$: for the QB case conduction (blue) and heat advection (red, dotted), for the AA and FC cases, we plot the conduction along the adiabat (red solid), and along the non-adiabatic temperature profile (blue), the work flow (green, dotted), the advection of enthalpy (red, dotted) is larger than when the enthalpy is identified with the temperature.

Figure S4. Quasi-Boussinesq and anelastic approximations, fully compressible case. Mean temperature (left-hand column) and density (right-hand column) profiles for $\mathcal{R} = 10^7$.

Figure S5. Same as Fig. A.3 for $\mathcal{R} = 10^7$

Figure S6. Quasi-Boussinesq and anelastic approximations. Mean temperature (left-hand column) and density (right-hand column) profiles for $\mathcal{R} = 10^8$.

Figure S7. Quasi-Boussinesq and anelastic approximations, fully compressible case. Mean temperature (left-hand column) and density (right-hand column) profiles for $\mathcal{R} = 10^9$.

Figure S8. Same as Fig. A.5 for $\mathcal{R} = 10^9$

Please note: Oxford University Press is not responsible for the content or functionality of any supporting materials supplied by the authors. Any queries (other than missing material) should be directed to the corresponding author for the paper.